

# Effects of Photoionization and Photoheating on Lyman- $\alpha$ Forest Properties from *Cholla* Cosmological Simulations

BRUNO VILLASENOR,<sup>1</sup> BRANT ROBERTSON,<sup>1</sup> PIERO MADAU,<sup>1</sup> AND EVAN SCHNEIDER<sup>2</sup>

<sup>1</sup>*Department of Astronomy and Astrophysics, University of California, Santa Cruz, 1156 High Street, Santa Cruz, CA 95064 USA*

<sup>2</sup>*Department of Physics and Astronomy & Pittsburgh Particle Physics, Astrophysics, and Cosmology Center (PITT PACC), University of Pittsburgh, Pittsburgh, PA 15260, USA*

## ABSTRACT

The density and temperature properties of the intergalactic medium (IGM) reflect the heating and ionization history during cosmological structure formation, and are primarily probed by the Lyman- $\alpha$  forest of neutral hydrogen absorption features in the observed spectra of background sources (Gunn & Peterson 1965). We present the methodology and initial results from the *Cholla* IGM Photoheating Simulation (CHIPS) suite performed with the Graphics Process Unit-accelerated *Cholla* code to study the IGM at high, uniform spatial resolution maintained over large volumes. In this first paper, we examine the IGM structure in CHIPS cosmological simulations that include IGM uniform photoheating and photoionization models where hydrogen reionization completes early (Haardt & Madau 2012) or by redshift  $z \sim 6$  (Puchwein et al. 2019). Comparing with observations of the large- and small-scale Lyman- $\alpha$  transmitted flux power spectra  $P(k)$  at redshifts  $2 \lesssim z \lesssim 5.5$ , the relative agreement of the models depends on scale, with the self-consistent Puchwein et al. (2019) IGM photoheating and photoionization model in good agreement with the flux  $P(k)$  at  $k \gtrsim 0.01 \text{ s km}^{-1}$  at redshifts  $2 \lesssim z \lesssim 3.5$ . On larger scales the  $P(k)$  measurements increase in amplitude from  $z \sim 4.6$  to  $z \sim 2.2$  faster than the models, and lie in between the model predictions at  $2.2 \lesssim z \lesssim 4.6$  for  $k \approx 0.002 - 0.01 \text{ s km}^{-1}$ . We argue the models could improve by changing the He II photoheating rate associated with active galactic nuclei to reduce the IGM temperature at  $z \sim 3$ . At higher redshifts  $z \gtrsim 4.5$  the observed flux  $P(k)$  amplitude increases at a rate intermediate between the models, and we argue that for models where hydrogen reionization completes late ( $z \sim 5.5 - 6$ ) resolving this disagreement will require inhomogeneous or “patchy” reionization. We then use an additional set of simulations to demonstrate our results have numerically converged and are not strongly affected by varying cosmological parameters.

**Keywords:** Hydrodynamical simulations (767) – Large-scale structure of the universe (902) – Lyman- $\alpha$  -forest (980) – Computational methods (1965)

## 1. INTRODUCTION

The absorption signatures of neutral hydrogen gas provide important observational probes of cosmological structure formation (Gunn & Peterson 1965). The intergalactic medium traces the filamentary structure of the cosmic web, and the properties of H I absorption features (the “Lyman- $\alpha$  forest”) reflect the temperature and density distribution of the medium that originate through the structure formation process and the photoheating from ionizing sources (e.g., Madau et al. 1999). This paper presents the first results from

the new *Cholla* IGM Photoheating Simulation (CHIPS) suite of cosmological simulations of the Lyman- $\alpha$  forest performed with the *Cholla* code (Schneider & Robertson 2015), comparing the statistics of the simulated Lyman- $\alpha$  forest calculated using different photoionization and photoheating histories with the available observational data at  $z \sim 2 - 5$ .

The Lyman- $\alpha$  forest originates in IGM gas that traces the matter density, and its properties inform us about the relative abundance of baryons and dark matter, the properties of dark matter including the matter power spectrum, the metagalactic radiation field, and the expansion history of the universe including the role of dark energy (for a review, see McQuinn 2016). The promise of the Lyman- $\alpha$  forest for constraining the nature of dark

matter and dark energy has in part motivated the construction of the Dark Energy Spectroscopic Instrument, which will measure absorption line spectra backlit by quasars at  $z > 2.1$  and detect baryon acoustic oscillations in the cosmic web (DESI Collaboration et al. 2016a,b).

Given its critical role as a probe of cosmic structure formation, the Lyman- $\alpha$  forest was an early subject of hydrodynamical cosmological simulations (e.g., Cen et al. 1994; Hernquist et al. 1996). The prospect of measuring quasar absorption spectra densely sampled on the sky over large statistical volumes has led to a resurgence of cosmic web studies in the literature (e.g., Lukić et al. 2015; Sorini et al. 2018; Krolewski et al. 2018). Owing to the power of DESI and other new spectroscopic facilities, the driving focus of theoretical efforts is to study the physics that affect the fine details of the forest (e.g., Rorai et al. 2017). These physics include non-linear effects (Arinyo-i-Prats et al. 2015), environment (Tonnesen et al. 2017), and how the forest evolves to low redshifts (Khaire et al. 2019), but a consensus is building that the impact of IGM heating history on the temperature structure of the Lyman- $\alpha$  forest is the most critical to understand in detail (e.g., Hiss et al. 2018). The temperature structure affects most strongly the shape of the absorption profiles that provide information about the matter distribution, and without understanding the thermal structure of filaments the full power of Lyman- $\alpha$  absorption line studies cannot be realized.

The statistical properties of the Lyman- $\alpha$  forest are primarily measured via the “transmitted flux power spectrum”, which probes fluctuations in the opacity (and therefore density, temperature and velocity field) of neutral hydrogen via transmission of flux from background quasars or galaxies. Similarly to the matter power spectrum, whose measurements extend to large ( $> 100$  Mpc comoving) scales via galaxy spatial correlations, the baryonic acoustic oscillations are probed by the Lyman- $\alpha$  forest correlations at these large scales as well (e.g., Chabanier et al. 2019). Structure in the Lyman- $\alpha$  forest extends down to scales of  $\sim 50$  kpc comoving, where thermal pressure smoothing becomes important (Kulkarni et al. 2015). Simultaneously capturing representative volumes while resolving the relevant spatial scales everywhere in the forest presents a challenging goal for cosmological simulations.

While dark matter and cosmological structure formation erect the scaffolding of the cosmic web, the temperature structure of the IGM depends on the competition between heating, radiative cooling, and adiabatic cooling via universal expansion. Heating of the IGM predominately occurs via photoheating from excess energy

deposited during the photoionization of (most importantly) the H I and He II species. Observationally, the Lyman- $\alpha$  forest probes redshifts  $z < 6$  when H I has mostly been ionized. Between  $4 \lesssim z \lesssim 6$ , the IGM temperature declines from a local maximum at the end of H I reionization from which the IGM thermal structure inherits residual signatures (Oñorbe et al. 2017b; Gnedin et al. 2017; Davies et al. 2018a; D’Aloisio et al. 2019; Faucher-Giguère 2020). At redshifts  $z \lesssim 4$ , photoheating from the gradual ionization of He II from quasars leads to a maximum IGM temperature sometime around  $z \sim 3$  (La Plante et al. 2017; Schmidt et al. 2018). The low-redshift ( $2 \lesssim z \lesssim 4$ ) IGM is therefore heavily influenced by He II reionization (Worseck et al. 2016), and the helium Lyman- $\alpha$  forest (La Plante et al. 2018) provides critical information on the ionizing flux from quasars (La Plante et al. 2017; Schmidt et al. 2018).

At higher redshifts the ionizing flux from galaxies becomes increasingly important. The various transitions of the hydrogen Lyman series provide details on the ionization state of the gas, and can constrain the post-reionization ionizing background (Davies et al. 2018a). The hydrogen reionization process heats the IGM sufficiently to leave residual signatures in the structure of the filaments (D’Aloisio et al. 2019). The thermal evolution of the IGM, reflecting early  $z \sim 6$  heating from galaxies during H reionization and late  $z \sim 2 - 4$  heating from QSOs during helium reionization, can therefore be probed through the Lyman- $\alpha$  forest power spectrum (Walther et al. 2019).

By changing the thermal history of the IGM, the process of cosmic reionization at  $z > 6$  couples to the observed properties of the Lyman- $\alpha$  forest on small scales. Probes of reionization have become increasingly powerful, including quasar proximity zones (Eilers et al. 2017) and the IGM damping wing (Davies et al. 2018b), the high-redshift forest and post-reionization IGM (Oñorbe et al. 2017b; Gnedin et al. 2017), and Lyman- $\alpha$  transmission spikes (Garaldi et al. 2019; Gaikwad et al. 2020b). The physics of reionization has driven a host of cosmological simulation efforts (e.g., Gnedin & Kaurov 2014; Kaurov & Gnedin 2014, 2015; Trac et al. 2015; Gnedin 2016; Oñorbe et al. 2017a; Doussot et al. 2019), but more work is required to connect these simulations to the physics of the IGM at lower redshifts. Capturing fluctuations in the metagalactic background (D’Aloisio et al. 2018) and the potential impact of rare AGN (D’Aloisio et al. 2017) require large volumes ( $L \sim 100h^{-1}\text{Mpc}$ ), but simultaneously maintaining high spatial resolution in the IGM is computationally demanding.

*Cholla* models the baryonic component on a uniform Cartesian grid, and while other approaches to solve the

hydrodynamics can be employed such as SPH or AMR, for which the computational power is commonly focused in solving the high density regions. These approaches present some disadvantages compared to a uniform grid when applied to the study of the IGM. For instance, the gas responsible for the Lyman- $\alpha$  forest is low density gas that spans over most of the volume of the box, making the use of AMR unnecessary and inefficient. Compared to an SPH approach, grid methods exhibit other advantages such as a clearly defined spatial resolution instead of a fixed mass resolution and generally a more accurate treatment of shocks and hydrodynamics. More importantly, a uniform grid achieves a better sampling of the IGM when compared to an AMR or SPH implementation that uses the same computational resources. Although, the advantages of a uniform grid come at a high computational cost if a high resolution is maintained over large volumes.

To this end, our new CHIPS simulation suite uses the Graphics Processing Unit (GPU)-native *Cholla* code (Schneider & Robertson 2015, 2017) to perform high-resolution simulations of the cosmic web to achieve simultaneously the resolution required to model the thermal structure of the Lyman- $\alpha$  forest ( $\Delta x \approx 35$  kpc) over large volumes ( $L \approx 75$  Mpc). We will study how different H I + He II photoionization and photoheating histories shape the thermal structure of the IGM.

This first paper presents Lyman- $\alpha$  forest results for the widely-used Haardt & Madau (2012) photoionization and photoheating model, as well as the more recent Puchwein et al. (2019) implementation that has a similar emissivity but for which H I reionization completes later ( $z \sim 6$ ). Section 2 presents our numerical methodology for performing the cosmological simulations including our new extensions to the *Cholla* code that enable, self-gravity, dark matter particle integration, and coupling to the GRACKLE heating and cooling library (Smith et al. 2017). Section 2.9 provides a high-level summary of the algorithm used in our cosmological simulations. Section 3 presents several validation tests, including a new validation test for the dual-energy formalism when modeling cosmological structure formation. We present the first simulations of the CHIPS suite in §4, including the cosmological parameters, resolution, and box sizes. Our scientific results for the properties of the IGM are reported in §5. We discuss our results in §6, and summarize and conclude in §7. Finally, we demonstrate the numerical convergence of our results in Appendix A and perform a cosmological parameter study in Appendix B

To simulate the Lyman- $\alpha$  -forest, we engineered substantial extensions to the *Cholla* code. These additions included implementing a cosmological framework to account for the expansion history of the universe (§2.1), including changes to the model of gas dynamics (§2.1.1) and the coordinate system (§2.1.2), and are discussed below. We briefly review the *Cholla* hydrodynamical integrator (§2.2) and the dual energy formalism (§2.3) that allows for accurate evolution of the gas internal energy in Eulerian cosmological simulations (e.g., Bryan et al. 1995). We present our new implementations of solvers for the gravitational force and particle motions in §2.4 and §2.5, respectively. Cooling and heating from a UV background are now treated using the GRACKLE library (Smith et al. 2017), and are detailed in §2.6 and §2.7. Adjustments to the time step calculation to account for particle motions are described in §2.8. We conclude the review of our methods with a summary of the overall algorithm in §2.9.

### 2.1. Cosmological Framework

For cosmological simulations, the gas follows the equations of hydrodynamics in a frame comoving with the expanding universe. To convert from the comoving to the physical system, the scale factor  $a$  is introduced and provides a distance transformation between the two systems, with coordinates in the proper system  $\mathbf{r}$  related to comoving coordinates  $\mathbf{x}$  by  $\mathbf{r} = a\mathbf{x}$ . The rate of change of the scale factor corresponds to the expansion rate of the universe and follows the Friedmann equation given by

$$H = \frac{\dot{a}}{a} = H_0 \sqrt{\frac{\Omega_M}{a^3} + \Omega_\Lambda + \frac{\Omega_k}{a^2}}, \quad (1)$$

where  $H$  is the Hubble parameter that quantifies the expansion rate of the universe  $\dot{a} = da/dt$ , and  $H_0$ ,  $\Omega_M$ ,  $\Omega_\Lambda$  and  $\Omega_k$  are the cosmological parameters that correspond to the current expansion rate of the universe and its matter, dark energy, and curvature content, respectively. Given an initial value of the scale factor  $a$ , the Friedmann equation provides a relation between the scale factor and cosmic time, and therefore the scale factor can be used as a time-like variable.

#### 2.1.1. Gas Dynamics

Consider the hydrodynamical quantities of comoving baryon density  $\rho_b$ , proper peculiar velocity  $\mathbf{v}$ , and total specific energy  $E$  in the proper frame. The relation between comoving and proper densities is  $\rho = a^3 \rho_{proper}$ . In this system, the basic equations of hydrodynamics include the continuity equation

$$\frac{\partial \rho_b}{\partial t} = -\frac{1}{a} \nabla \cdot (\rho_b \mathbf{v}), \quad (2)$$

## 2. METHODOLOGY

the force-momentum equation

$$\frac{\partial a \rho_b \mathbf{v}}{\partial t} = -\nabla \cdot (\rho_b \mathbf{v} \mathbf{v}) - \nabla p + \rho_b \mathbf{g}, \quad (3)$$

where the pressure  $p$  transforms to the proper pressure by the relation  $p = a^3 p_{proper}$  and  $\mathbf{g}$  is the gravitational acceleration, and the energy equation

$$\begin{aligned} \frac{\partial a^2 \rho_b E}{\partial t} = & -a \nabla \cdot (\rho_b \mathbf{v} E + p \mathbf{v}) + a \rho_b \mathbf{v} \cdot \mathbf{g} \\ & + a \dot{a} [(2 - 3(\gamma - 1)) \rho_b e] + a(\Gamma - \Lambda), \end{aligned} \quad (4)$$

where  $\Gamma$  and  $\Lambda$  correspond to the heating and cooling rates, respectively.

From the specific total energy one can obtain the specific internal energy  $e$  in the proper system by subtracting the kinetic energy per unit mass  $e = E - v^2/2$ . In Eulerian cosmological simulations where gas often flows supersonically, the above equations can be supplemented by a dual energy formalism (Bryan et al. 1995) in which the internal energy is additionally followed. The supplemental internal energy is then used in cells where the computation of the internal energy from the total energy is expected to be inaccurate (see §2.3 for details).

The evolution of the specific internal energy  $e$  is given by

$$\begin{aligned} \frac{\partial a^2 \rho_b e}{\partial t} = & -a \nabla \cdot (\rho_b \mathbf{v} e) - a p \nabla \cdot \mathbf{v} \\ & + a \dot{a} [(2 - 3(\gamma - 1)) \rho_b e] + a(\Gamma - \Lambda) \end{aligned} \quad (5)$$

The relation between the pressure and the internal energy is given by the equation of state  $p = (\gamma - 1) \rho_b e$ .

For simplicity, first we limit the description of the hydrodynamics solver to the adiabatic case ( $\Gamma = \Lambda = 0$ ), and delay a description of the radiative cooling implementation to §2.6. In the particular case of a  $\gamma = 5/3$  gas, the adiabatic energy equations simplify to

$$\begin{aligned} \frac{\partial a^2 \rho_b E}{\partial t} &= -a \nabla \cdot (\rho_b \mathbf{v} E + p \mathbf{v}) + a \rho_b \mathbf{v} \cdot \mathbf{g}, \\ \frac{\partial a^2 \rho_b e}{\partial t} &= -a \nabla \cdot (\rho_b \mathbf{v} e) - a p \nabla \cdot \mathbf{v}. \end{aligned} \quad (6)$$

From Equations 2, 3, and 6 it follows that for a uniform expanding universe, the comoving density  $\rho_b$  will remain constant, the peculiar velocity  $\mathbf{v}$  will decrease as  $a^{-1}$  and the specific energies  $E$  and  $e$  will decrease as  $a^{-2}$ .

### 2.1.2. Super-comoving Coordinates

A convenient approach for the implementation of the comoving coordinate system is to define a new set of coordinates that simplify Equations 2, 3, and 6 such that the scale factor  $a$  does not explicitly appear. A detailed

description of these “super-comoving coordinates” can be found in Martel & Shapiro (1998) and are used for cosmological simulations in the *Ramses* code by Teyssier (2002). The transformation to the new system of coordinates is given by

$$\begin{aligned} d\tilde{t} &\equiv H_0 \frac{dt}{a^2}, & \tilde{\mathbf{v}} &\equiv a \frac{\mathbf{v}}{H_0}, \\ \tilde{E} &\equiv a^2 \frac{E}{H_0^2}, & \tilde{e} &\equiv a^2 \frac{e}{H_0^2}, \\ \tilde{\rho}_b &\equiv \rho_b, & \tilde{p} &\equiv a^2 \frac{p}{H_0^2} = (\gamma - 1) \tilde{\rho}_b \tilde{e}, \\ \tilde{\phi} &\equiv a^2 \frac{\phi}{H_0^2}, & \tilde{\mathbf{g}} &= -\nabla \tilde{\phi} = a^2 \frac{\mathbf{g}}{H_0^2}. \end{aligned} \quad (7)$$

Throughout we will denote super-comoving variables with a tilde, e.g.,  $\tilde{\phi}$ . After the transformation to the super-comoving system of coordinates, the equations of adiabatic hydrodynamics for a  $\gamma = 5/3$  gas can be written as

$$\frac{\partial \tilde{\rho}_b}{\partial \tilde{t}} = -\nabla \cdot (\tilde{\rho}_b \tilde{\mathbf{v}}) \quad (8)$$

$$\frac{\partial \tilde{\rho}_b \tilde{\mathbf{v}}}{\partial \tilde{t}} = -\nabla \cdot (\tilde{\rho}_b \tilde{\mathbf{v}} \tilde{\mathbf{v}}) - \nabla \tilde{p} + \tilde{\rho}_b \tilde{\mathbf{g}} \quad (9)$$

$$\frac{\partial \tilde{\rho}_b \tilde{E}}{\partial \tilde{t}} = -\nabla \cdot (\tilde{\rho}_b \tilde{\mathbf{v}} \tilde{E} + \tilde{p} \tilde{\mathbf{v}}) + \tilde{\rho}_b \tilde{\mathbf{v}} \cdot \tilde{\mathbf{g}} \quad (10)$$

$$\frac{\partial \tilde{\rho}_b \tilde{e}}{\partial \tilde{t}} = -\nabla \cdot (\tilde{\rho}_b \tilde{\mathbf{v}} \tilde{e}) - \tilde{p} \nabla \cdot \tilde{\mathbf{v}} \quad (11)$$

The set of equations resulting from the transformation are the same as the original equations of hydrodynamics in a non-expanding system. This formulation allows the extension of the hydrodynamics solver to an expanding frame system without any significant changes to the original solver.

### 2.2. Hydrodynamics Solver

Without the gravitational source terms, Equations 8–11 correspond to the conserved form of the Euler equations. A detailed description of the methodology used for solving the gravity-free fluid dynamics can be found in Schneider & Robertson (2015). The hydrodynamics solver is a Godunov-based method for which an approximation to the cell averaged values of the conserved quantities  $\mathbf{U} = [\rho, \rho \mathbf{v}, \rho E, \rho e]$  are evolved using a numerical discretization of the Euler equations, given by

$$\frac{\mathbf{U}_i^{n+1} - \mathbf{U}_i^n}{\Delta t} + \frac{\mathbf{F}_{i+1/2}^{n+1/2} - \mathbf{F}_{i-1/2}^{n+1/2}}{\Delta x} = 0 \quad (12)$$

where  $\mathbf{U}_i^n$  denotes the average value of the conserved quantities for cell  $i$  at time-step  $n$ . The change of the conserved quantities in cell  $i$  is given by the time centered fluxes across the cell interfaces  $\mathbf{F}_{i\pm 1/2}^{n+1/2}$ . The flux



components  $\mathbf{F} = [\rho\mathbf{v}, \rho\mathbf{v}\mathbf{v}, (\rho E + p)\mathbf{v}, \rho e\mathbf{v}]$  are computed by solving the Riemann problem at the cell interfaces using the reconstructed values of the conserved quantities obtained via a Piecewise Parabolic Method (PPM; Colella & Woodward 1984). The PPM scheme is third-order accurate in space and second-order accurate in time.

### 2.3. Dual Energy Implementation

Owing to the supersonic flows from structure formation and adiabatic cooling of gas from universal expansion, regions where the gas kinetic energy is much larger than the internal energy are common in cosmological simulations. Under these conditions, calculation of the internal energy  $E - v^2/2$  can be affected by numerical errors. These errors can be ameliorated by using a “dual energy formalism” (Bryan et al. 1995), where the internal energy is evolved separately via Equation 5, or the corresponding simplified Equation 11, and substituted for the internal energy computed from the total and kinetic energies when appropriate. The two terms on the right side of Equation 11 correspond to advection and compression terms, respectively. To reconcile the total internal energy  $E$  with the separately tracked internal energy  $e$ , at the end of each time step a condition is applied on a cell to cell basis to select which value of the internal energy to employ. We adopt a condition similar to that used in *Enzo* (Bryan et al. 2014), where the selection is based on the fraction of the internal energy in a given cell relative to the maximum of the total energy in a the neighborhood of the cell. Mathematically, this condition is given by

$$e_i = \begin{cases} e_i, & \rho_i (E - v^2/2)_i / \max(\rho E)_i < \eta \\ (E - v^2/2)_i, & \text{otherwise} \end{cases}, \quad (13)$$

where  $\max(\rho E)_i$  is the maximum total specific energy in the local and adjacent cells. In one dimension,  $\max(\rho E)_i = \max[(\rho E)_{i-1}, (\rho E)_i, (\rho E)_{i+1}]$ . At the end of every time step, after applying Equation 13, the total specific energy  $E$  is synchronized with the selected internal energy by setting  $E = e + v^2/2$ .

The value of  $\eta$  should be chosen carefully, as setting  $\eta$  too low will allow spurious heating owing to numerical errors introduced in the total energy evolution. If  $\eta$  is set to high then shock heating in regions where the gas flows converge could be suppressed since the advected internal energy  $e$  will be preferentially selected over the conserved internal energy  $E - v^2/2$ , and Equations 5 and 11 do not capture shock heating. To estimate an appropriate value for  $\eta$  in cosmological simulations, we developed a test to evaluate how the dual energy condition affects the average cosmic gas temperature, as

described below in §3.4. Based on the results of this test, we set  $\eta = 0.035$ .

Another approach on the selection criteria for the internal energy is presented in Teyssier (2015). Here, the conserved internal energy  $\rho(E - v^2/2)$  is compared to an estimate of the numerical truncation error

$$e_{\text{trunc}} \simeq \frac{1}{2}\rho(\Delta v)^2, \quad (14)$$

where  $\Delta v$  corresponds to the difference of the velocities in the neighboring cells. The selection condition for this scheme is given by

$$e_i = \begin{cases} (E - v^2/2)_i, & \rho_i (E - v^2/2)_i > \beta e_{\text{trunc}} \\ e_i, & \text{otherwise} \end{cases}, \quad (15)$$

where  $\beta$  is a numerical parameter with suggested value  $\beta = 0.5$ . We also evaluated this dual energy condition using the average cosmic temperature test described in §3.4. As we discuss below, we found that Equation 15 can be overly restrictive by predominately selecting the advected internal energy  $e$  over the conserved internal energy  $E - v^2/2$ , thereby suppressing shock heating inside collapsed halos and significantly lowering the average cosmic temperature.

### 2.4. Gravity

The gravitational acceleration vector  $\mathbf{g}$  is computed by differentiating the gravitational potential  $\phi$ . The potential is obtained from the solution of the Poisson equation. In the comoving coordinates, the Poisson equation is written as

$$\nabla^2 \phi = \frac{4\pi G}{a}(\rho - \bar{\rho}), \quad (16)$$

where  $G$  is the gravitational constant,  $\rho = \rho_{\text{DM}} + \rho_b$  is the total dark plus baryonic matter density, and  $\bar{\rho}$  is the average value of the total density over the entire box.

Integration of Equation 16 can be directly performed in Fourier space. In  $k$ -space, the Poisson equation simplifies to

$$\hat{\phi}(\mathbf{k}) = G(\mathbf{k})\hat{\rho}(\mathbf{k}), \quad (17)$$

where  $G(\mathbf{k})$  is the Greens function, which for a second-order centered two point finite difference discretization corresponds to (Hockney & Eastwood 1988)

$$G(\mathbf{k}) = -\frac{\Delta x_h^2}{\sin^2(k_x \Delta x_h)} - \frac{\Delta y_h^2}{\sin^2(k_y \Delta y_h)} - \frac{\Delta z_h^2}{\sin^2(k_z \Delta z_h)}. \quad (18)$$

Here  $\Delta x_h = \Delta x/2$ ,  $\Delta y_h = \Delta y/2$ , and  $\Delta z_h = \Delta z/2$ , where  $\Delta x$ ,  $\Delta y$ , and  $\Delta z$  are the grid cell dimensions. To compute the three-dimensional fast Fourier transforms

(FFTs) we use *PFFT* (Pippig 2013), a publicly available library for performing FFTs with a box domain decomposition.

From the potential  $\phi$  we compute the gravitational acceleration vector  $\mathbf{g} = -\nabla\phi$ . The derivatives along each direction are obtained using a fourth-order centered four-point finite difference approximation. In one dimension, the derivative is given by

$$\frac{\partial\phi_i}{\partial x} = \frac{1}{12\Delta x} (\phi_{i-2} - 8\phi_{i-1} + 8\phi_{i+1} - \phi_{i+2}). \quad (19)$$

The terms corresponding to the gravitational sources,  $\tilde{\rho}_b \tilde{\mathbf{g}}$  and  $\tilde{\rho}_b \tilde{\mathbf{v}} \cdot \tilde{\mathbf{g}}$  in Equations 9 and 10, are added to the momentum and total energy after the conserved variables have been updated by the hydro solver (i.e., after Equation 12 has been solved). The numerical implementation for the coupling of the momentum and energy with gravity is given by

$$(\tilde{\rho}_b \tilde{\mathbf{v}})_i^{n+1} = (\tilde{\rho}_b \tilde{\mathbf{v}})_i^{n+1*} + \frac{1}{2} \Delta t^n \left( \tilde{\rho}_{b,i}^n + \tilde{\rho}_{b,i}^{n+1} \right) \tilde{\mathbf{g}}_i^{n+1/2}, \quad (20)$$

$$(\tilde{\rho}_b \tilde{E})_i^{n+1} = (\tilde{\rho}_b \tilde{E})_i^{n+1*} + \frac{1}{2} \Delta t^n \left[ (\tilde{\rho}_b \tilde{\mathbf{v}})_i^n + (\tilde{\rho}_b \tilde{\mathbf{v}})_i^{n+1*} \right] \tilde{\mathbf{g}}_i^{n+1/2}. \quad (21)$$

Here the superscript  $n+1*$  refers to the value of the conserved quantity after the hydrodynamics solver update and the time centered value of the gravitational field  $\tilde{\mathbf{g}}_i^{n+1/2} = -\nabla \tilde{\phi}_i^{n+1/2}$ . The potential  $\tilde{\phi}_i^{n+1/2}$  is obtained by extrapolation from  $\phi_i^n$  and  $\phi_i^{n-1}$  using

$$\tilde{\phi}_i^{n+1/2} = \frac{(a^n)^2}{H_0^2} \left[ \phi_i^n + \frac{\Delta t^n}{2\Delta t^{n-1}} (\phi_i^n - \phi_i^{n-1}) \right]. \quad (22)$$

### 2.5. Dark Matter

We represent the cold dark matter as a system of discrete point-mass particles moving under the influence of gravity. Each dark matter particle is described by its mass  $m_i$ , comoving position  $\mathbf{x}_i$ , and peculiar velocity  $\mathbf{v}_i$ . The evolution of the particle trajectories in a comoving frame is described by

$$\frac{d\mathbf{x}_i}{dt} = \frac{1}{a} \mathbf{v}_i \quad (23)$$

$$\frac{d(a\mathbf{v}_i)}{dt} = \mathbf{g}_i, \quad (24)$$

where  $\mathbf{g}_i$  is the acceleration vector owing to the gravitational field evaluated at the particle position  $\mathbf{x}_i$ .

To solve Equation 16, we compute the contribution of the dark matter particles to the density field by interpolating onto the same grid used to evolve the hydrodynamical quantities. The dark matter density  $\rho_{\text{DM}}$  is calculated via a cloud-in-cell scheme (Hockney & Eastwood

1988), for which each particle is represented as a cube having the same size as one grid cell  $\Delta x$  and uniform density  $m_i/\Delta x^3$ . The mass of the particle is distributed among the grid cells that intersect its volume such that the fraction of the particle mass  $\delta m_i$  deposited on a cell is equal to the fraction of its intersected volume.

In one dimension, the mass contribution of a particle to a cell at position  $x_c$  is given by

$$\delta m_{i,c} = m_i \begin{cases} 1 - |x_i - x_c|/\Delta x, & |x_i - x_c| < \Delta x \\ 0, & \text{otherwise} \end{cases}. \quad (25)$$

The gravitational acceleration  $\mathbf{g}_i$  evaluated at a particle position  $\mathbf{x}_i$  must be computed in a manner consistent with the particle density interpolation. For the cloud-in-cell scheme, to avoid self-forces on the particles each component of  $\mathbf{g}$  should be interpolated with the same weights used during the density assignment calculation.

To integrate the particle trajectories we use the kick-drift-kick (KDK) method (Miniati & Colella 2007), consisting of three steps to update the particles position and velocity from time-step  $n$  to time-step  $n+1$ . The sequence of variable updates is

$$\mathbf{v}_i^{n+1/2} = \frac{1}{a^{n+1/2}} \left( a^n \mathbf{v}_i^n + \frac{\Delta t^n}{2} \mathbf{g}_i^n \right), \quad (26)$$

$$\mathbf{x}_i^{n+1} = \mathbf{x}_i + \frac{\Delta t^n}{a^{n+1/2}} \mathbf{v}_i^{n+1/2}, \quad (27)$$

$$\mathbf{v}_i^{n+1} = \frac{1}{a^{n+1}} \left( a^{n+1/2} \mathbf{v}_i^{n+1/2} + \frac{\Delta t^n}{2} \mathbf{g}_i^{n+1} \right). \quad (28)$$

The KDK scheme allows for variable timesteps, as required by cosmological simulations owing to the variation in gas and particles velocities as the simulation advances. This symplectic scheme conserves an integral of motion on average, preventing an accumulation of errors and maintaining the phase space trajectory of the particles.

### 2.6. Chemistry and Radiative Cooling

We integrated *Cholla* with the GRACKLE chemistry and cooling library (Smith et al. 2017) to solve a non-equilibrium chemical network. Currently, our method only tracks the atomic chemical species and metals, but it could be extended to include, e.g., molecular hydrogen and deuterium.

The chemical species (H I, H II, He I, He II, He III, electrons  $e^-$ , and metals Z) are advected as scalar fields alongside the gas conserved variables via Equation 12. For details about the implementation of GRACKLE, we refer the reader to Smith et al. (2017). During every time step, GRACKLE updates the ionization fractions and computes the net heating and cooling by sub-cycling

the rate equations within one hydrodynamic step. The sub-cycling updates the chemical and thermal states of the gas on timescales smaller than the dynamical timescales. For the atomic H and He chemical network, GRACKLE directly computes the heating and cooling rates accounting for collisional excitation and ionization, recombination, free-free emission, Compton scattering from the cosmic microwave background, and photoheating from a metagalactic UV background. GRACKLE accounts for metals by using precomputed tables for the metallic cooling and heating rates.

The GRACKLE update routine is applied at the end of each time step, after the gas conserved variables have been updated by the hydro solver and additional gravitational source terms. This routine updates the ionization fraction of the chemical elements, and also adds the net cooling and heating to the internal energy by setting

$$(\rho e)_i^{n+1} \rightarrow (\rho e)_i^{n+1} + a \Delta t^n (\Gamma - \Lambda)_i^n \quad (29)$$

Finally, the total energy is updated to reflect the change in the internal energy due to the net cooling as

$$E_i^{n+1} = \frac{1}{2}(v_i^{n+1})^2 + e_i^{n+1}. \quad (30)$$

### 2.7. UVB Ionization and Heating

The non-equilibrium GRACKLE solver accounts for the ionization of the primordial chemical species owing to a uniform time-dependent UV background by loading tables of the redshift dependent photoionization and photoheating rates for H I, He I, and He II. We compute the photoionization rates from a given redshift dependent spectrum as

$$\Gamma_{\gamma i}(z) = \int_{\nu_i}^{\infty} \frac{4\pi J(\nu, z)}{h\nu} \sigma_i(\nu) d\nu, \quad (31)$$

where  $J(\nu, z)$  is the intensity of the UV background at frequency  $\nu$  (in  $\text{erg s}^{-1} \text{cm}^{-2} \text{sr}^{-1} \text{Hz}^{-1}$ ), and  $\nu_i$  and  $\sigma_i(\nu)$  are the threshold frequency and cross-section for photoionization of the species  $i$ , taken from [Osterbrock \(1989\)](#). Analogously, the photoheating rates are computed as

$$\epsilon_i(z) = \int_{\nu_i}^{\infty} \frac{4\pi J(\nu, z)}{h\nu} (h\nu - h\nu_i) \sigma_i(\nu) d\nu. \quad (32)$$

If metal line cooling is included, the contributions of metals to the heating and cooling rates are accounted by GRACKLE by loading precomputed density, temperature and redshift dependent lookup tables that were obtained by providing the UVB spectrum to the CLOUDY ([Ferland et al. 2017](#)) photoionization code (version 17.02). The tables for metallic heating and

cooling rates were generated for solar metallicity under the assumption of ionization equilibrium and subtracting the contributions of primordial heating and cooling as described in [Smith et al. \(2017\)](#). The resulting tables are organized into a Hierarchical Data Format (version 5) file readable by GRACKLE.

### 2.8. Time Step Calculation

The simulation time step  $\Delta t$  is computed with constraints from the signal speed of the gas, the motion of the dark matter particles, and the expansion of the universe. For the gas, the time step is constrained by the gas velocities  $\mathbf{v}$  and the sound speed  $c_s$  as

$$\Delta t_{\text{gas}} = \alpha_{\text{gas}} \min \left( \frac{a\Delta x}{|v_x| + c_s}, \frac{a\Delta y}{|v_y| + c_s}, \frac{a\Delta z}{|v_z| + c_s} \right), \quad (33)$$

where  $\alpha_{\text{gas}}$  is the CFL factor specified by the user ( $\alpha_{\text{gas}} = 0.3$  by default) and  $|v| + c_s$  is evaluated over the entire grid for each direction to find the minimum value of  $\Delta t_{\text{gas}}$ . For the particles, the time step is limited to avoid any displacement larger than the cell size in each direction using

$$\Delta t_{\text{DM}} = \alpha_{\text{DM}} \min \left( \frac{a\Delta x}{|v_x|}, \frac{a\Delta y}{|v_y|}, \frac{a\Delta z}{|v_z|} \right), \quad (34)$$

where  $\alpha_{\text{DM}}$  is analogous to the CFL factor ( $\alpha_{\text{DM}} = 0.3$  by default) and  $|v|$  is evaluated over all the particles for each direction. The time step is also limited by the expansion of the universe by choosing  $\Delta t_{\text{exp}}$  such that the fractional change in the scale factor does not exceed 1% ( $\Delta a_{\text{exp}} = 0.01a$ ). The actual time step is selected by taking the smallest value

$$\Delta t = \min(\Delta t_{\text{gas}}, \Delta t_{\text{DM}}, \Delta t_{\text{exp}}), \quad (35)$$

guaranteeing that all three limiting conditions described above are satisfied.

The time step  $\Delta t$  (Eq. 35) is applied globally to update all the cells and particles in the box. When running high resolution simulations, it is possible to have a situation in which for a single cell  $\Delta t_{\text{gas},i}$  is extremely small compared to the all the other cells, resulting in small values for  $\Delta t$  which significantly slow the entire simulation. To avoid this situation, when a cell satisfies the condition  $\Delta t_{\text{gas},i} < \Delta t_{\text{DM}}/50$  then the conserved quantities of that cell (density, momentum, energy, and internal energy) are replaced with the conserved quantities averaged over the six closest neighboring cells, resulting in a larger  $\Delta t_{\text{gas},i}$  for such cell and avoiding extremely small steps. We keep track of this occurrences during the full run, and for the high resolution simulations presented in this work this situation happens less than a

dozen times per simulation, ensuring that the dynamics of the gas are not significantly affected by these small interventions.

### 2.9. Algorithm Implementation

The complete method to evolve the gas and the dark matter particles from time-step  $n$  to time-step  $n+1$  can be summarized by the following algorithm:

#### Initialization:

1. Load initial conditions for the gas conserved variables and the particle positions and velocities.
2. Obtain the dark matter density  $\rho_{\text{DM}}$  by interpolating the particle masses onto the grid via the Cloud-In-Cell method described in §2.5.
3. Compute the gravitational potential  $\phi$  by solving the Poisson equation (Eqn. 16), using the dark matter density  $\rho_{\text{DM}}$  and the gas density  $\rho_b$  as the sources.
4. Calculate the gravitational field  $\mathbf{g} = -\nabla\phi$  at the centers of the grid cells using a fourth-order finite difference scheme (Eqn. 19) and interpolate the acceleration vector evaluated at the particles positions  $\mathbf{g}_i = \mathbf{g}(\mathbf{x}_i)$ .

#### Time Step Update:

1. Compute the current time step  $\Delta t^n$ .
2. Obtain the gravitational potential at  $t^{n+1/2}$  by extrapolation using  $\phi^n$  and  $\phi^{n-1}$ , Equation 22.
3. Advance the gas conserved quantities by  $\Delta t^n$  using the intercell fluxes  $\mathbf{F}^{n+1/2}$ , Equation 12.
4. Add the gravitational sources to the gas momentum and energy, Equation 20.
5. Call GRACKLE to update the ionization states of the chemical network and add the net cooling and heating to the internal energy, Equation 29.
6. Advance the particle velocities by  $\frac{1}{2}\Delta t^n$  and use the updated velocities  $\mathbf{v}_i^{n+1/2}$  to advance the particle positions by  $\Delta t^n$ , Equations 26 and 27.
7. Obtain the dark matter density  $\rho_{\text{DM}}^{n+1}$  via the CIC method.
8. Compute the gravitational potential  $\phi^{n+1}$  by solving Equation 16 with  $\rho_{\text{DM}}^{n+1}$  and  $\rho_b^{n+1}$  as sources.
9. Obtain the gravitational field  $\mathbf{g}^{n+1}$  at the cell centers and  $\mathbf{g}_i^{n+1}$  evaluated at the particle positions.

10. Advance the particle velocities by  $\frac{1}{2}\Delta t^n$  resulting in  $\mathbf{v}_i^{n+1}$ , Equation 28.

Currently, the extensions included into *Cholla* for cosmological simulations (the FFT based Poisson solver, the dark matter particles integrator and the chemical network solver) all are implemented to run in the host CPUs, while the hydrodynamics solver including the advection of the ionization states of H and He run in the GPUs. At the time of submission of this work, an entirely GPU based distributed FFT solver has been recently integrated into *Cholla* and development to transfer both the particle integrator and the H+He network solver to the GPUs is ongoing. Potentially, the GPU implementation of a H+He network solver analogous to GRACKLE could result in a significant performance increase since currently the GRACKLE call to update the chemical network is the slowest step in our implementation.

### 3. VALIDATION

To test the extensions of the *Cholla* code for cosmological simulations, we present below a set of validation exercises including comparisons with other publicly available Eulerian codes. In §3.1 we present the standard Zel'Dovich (1970) test. We then compare in §3.2 the matter power spectra of N-body cosmological simulations performed with *Cholla* to results from the *Nyx* (Almgren et al. 2013), *Ramsey* (Teyssier 2002), and *Enzo* (Bryan et al. 2014) codes using the same initial conditions, and find sub-percent-level agreement at all spatial scales when simulated with the same resolution. We extend these tests to adiabatic hydrodynamical cosmological simulations in §3.3, where we find agreement within a few percent. To test the dual energy formalism in cosmological simulations, we describe a new test that computes the mean gas temperature with redshift (§3.4), and show that our choice of dual energy parameterization and parameter values recovers model expectations. We validate our cosmological hydrodynamical simulations including cooling, chemistry, and heating against *Enzo* simulations using the same physical prescription, and find good agreement.

#### 3.1. Zel'Dovich Pancake

The Zel'Dovich (1970) pancake problem encompasses several of the basic components of a cosmological hydrodynamical simulation including gas dynamics, self-gravity, and an expanding frame. For this test, the evolution of a single one dimensional sinusoidal perturbation is followed to provide a useful representation of the gas evolution in a three-dimensional simulation by solving the gravitational collapse of a single mode. The ini-



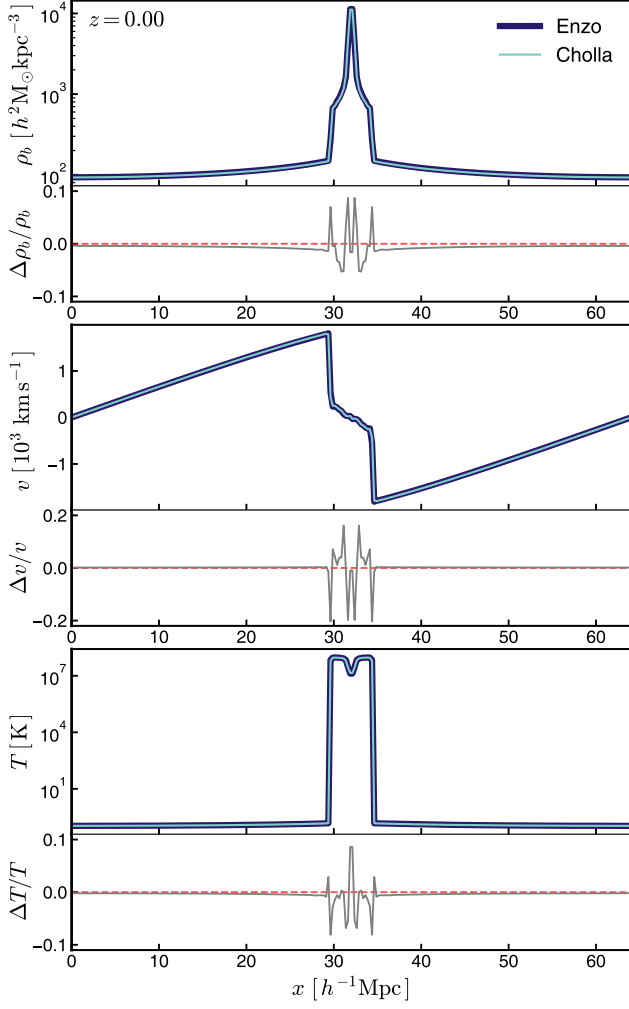


**Figure 1.** Zel'Dovich pancake test at  $z = 0$  for a one dimensional  $64 h^{-1}\text{Mpc}$  box discretized on a 256 uniform grid for a  $h = 0.5$  and  $\Omega_M = 1$  universe. Shown are the solutions computed using *Enzo* (purple) and *Cholla* (blue). The top, middle, and bottom main panels correspond to the density ( $\rho_b$ ), velocity ( $v$ ), and temperature ( $T$ ), respectively, the fractional differences for each quantity are shown at the bottom of each panel (gray lines). The *Cholla* simulations resolve the central shock and overdensity, and the results are in excellent agreement with the *Enzo* simulation. Small differences  $< 10\%$  for  $\rho_b$  and  $T$  are located at the sharp features of the shock, and differences  $\sim 20\%$  for  $v$  at the regions where  $v \sim 0$  and at the fronts of the shock.

tial conditions for the density, velocity and temperature

on a Lagrangian frame are set as

$$\rho_b(x_l) = \rho_0 \left[ 1 - \frac{1+z_s}{1+z} \cos(kx_l) \right]^{-1} \quad (36)$$

$$v(x_l) = -H_0 \frac{1+z_s}{(1+z)^{1/2}} \frac{\sin(kx_l)}{k} \quad (37)$$

$$T(x_l) = T_0 \left[ \frac{\rho_b(x_l)}{\bar{\rho}_b} \right]^{2/3}, \quad (38)$$

where  $z_s$  is the value of the redshift at which the gravitational collapse results in the formation of a shock located at the center of the overdensity,  $z$  is the initial redshift,  $\lambda$  is the wavelength of the perturbation,  $k = 2\pi/\lambda$  is the corresponding wavenumber, and  $x_l$  is the position of the Lagrangian mass coordinate. The conversion of the positions to the Eulerian coordinates  $x$  is given by

$$x = x_l - \frac{1+z_s}{1+z} \frac{\sin(kx_l)}{k}. \quad (39)$$

For this test we replicate the problem presented in [Bryan et al. \(2014\)](#), a one dimensional simulation on an  $L = 64 h^{-1}\text{Mpc}$  box with cosmological parameters  $h = 0.5$  and  $\Omega_M = 1$ . The initial background density and temperature ( $\rho_0$  and  $T_0$ ) are set equal to the critical density  $\rho_c = 3H_0^2/8\pi G$  and 100 K respectively. The redshift at which the shock develops is set as  $z_s = 1$  and the wavelength of the perturbation is set as  $\lambda = L = 64 h^{-1}\text{Mpc}$ . The simulation is initialized at  $z = 20$  and runs on an  $N = 256$  cell uniform grid.

Comparing the evolution of the Zel'dovich pancake problem solved using *Cholla* and *Enzo*, we find the results from the *Cholla* simulation closely resemble the *Enzo* results. Both simulations develop a central shock at  $z = 1$  and the central overdensity grows at the same rate. Figure 1 compares the density  $\rho_b$ , velocity  $v$  and temperature  $T$  fields at  $z = 0$  in the simulations solved with *Enzo* (purple lines) and *Cholla* (blue lines), additionally, the fractional differences are shown at the bottom of each panel (gray lines). We measure small differences  $< 10\%$  for the density and the temperature only at the sharp features of the shock. For the velocity the differences are  $\sim 20\%$  at the discontinuities located at the front of the shock, and at the regions where  $v \sim 0$ , the other regions contained by the shock show small differences  $< 10\%$ . The regions outside the shock result in differences  $< 1\%$  for all the fields. The small differences demonstrate an excellent agreement between the codes.

We note that we also performed the Zel'Dovich pancake test by applying Equation 15 for the internal energy selection in the dual energy scheme. This condition causes the code to select the advected internal energy  $e$  instead of the conserved internal energy  $E - v^2/2$  during the entire simulation. Since Equation 5 does not

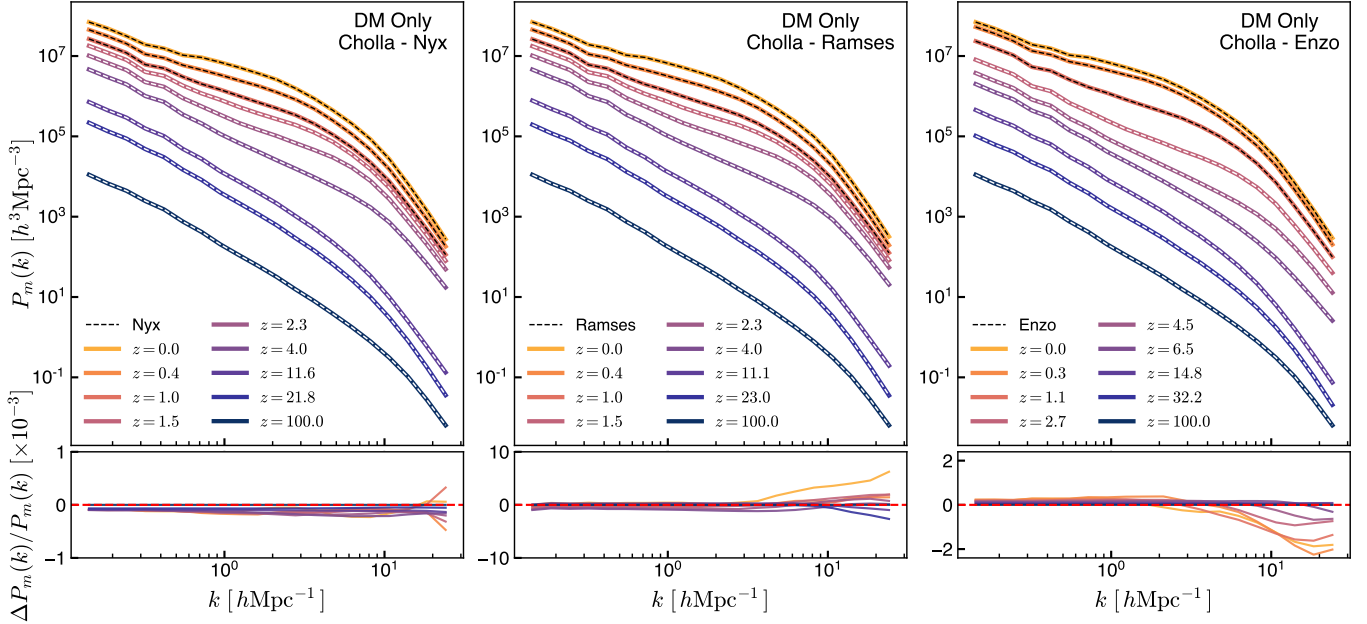


**Figure 2.** Matter power spectrum  $P_m(k)$  from dark matter-only simulations. Shown are  $P_m(k)$  from simulations performed with *Cholla* (colored lines) compared with analogous simulations computed with *Nyx*, *Ramses*, and *Enzo* (left, center, and right panels; dashed lines). The bottom panels show the fractional difference between the *Cholla* simulation and each corresponding code for comparison. For each of the comparison codes, the fractional differences relative to the *Cholla* results are  $< 0.1\%$  compared with *Nyx* (bottom left),  $< 1\%$  compared with *Ramses* (bottom center), and  $< 0.3\%$  compared with *Enzo* (bottom right).

captures shock heating, the central shock at  $z = 1$  is suppressed and the temperature of the central region only gradually increases owing to the gas compression. This behavior results in a significantly different distribution for the density, velocity, and temperature in the central region. We discuss further ramifications of the dual energy condition in §3.4.

### 3.2. *N-body Cosmological Simulations*

To validate the results produced by *Cholla* in a realistic cosmological setting, first we compare *Cholla* dark matter-only simulations with calculations using several other well-established codes. In this test, the simulation domain consists of an  $L = 50(h^{-1}\text{Mpc})^3$  box. The standard cosmological parameters are set to  $\Omega_M = 0.3111$ ,  $\Omega_\Lambda = 0.6889$ ,  $h = 0.6766$ , and  $\sigma_8 = 0.8102$ . Initial conditions were generated at  $z = 100$  on a uniform resolution grid using the MUSIC software (Hahn & Abel 2011). For this test, we evolve  $256^3$  particles on an  $N = 256^3$  cell uniform grid, with the particle mass resolution equal to  $m_p = 6.4345 \times 10^8 h^{-1} \text{M}_\odot$ .

For our validation test, we measure the matter power spectrum  $P_m(k)$  evolved from identical initial conditions using *Cholla*, *Nyx* (Almgren et al. 2013), *Ramses* (Teyssier 2002), and *Enzo* (Bryan et al. 2014). To measure the matter power spectrum for each simulation, we first compute the dark matter density field by inter-

polating the dark matter particles onto the  $N = 256^3$  uniform grid via the CIC method described in §2.5. The power spectrum is then computed in Fourier space by taking the FFT of the overdensity field. The density field and power spectrum are computed identically for all the comparison simulations to ensure that any power spectrum differences arise solely from differences in the evolved particle distribution.

The results of our comparison are presented in Figure 2. Each panel in the upper row shows the matter power spectrum  $P_m(k)$  for several redshifts as computed by *Cholla* (colored lines), along with an overlay of the results from other codes (dashed lines). The left panel shows the comparison to the *Nyx* simulation, the center panel corresponds to the *Ramses* comparison, and the right panel shows the comparison to the *Enzo* results. The bottom row shows the fractional difference between the power spectrum of the simulation computed by *Cholla* and each comparison code. As the left lower panel shows, the power spectrum measured in the *Cholla* and *Nyx* simulations is in excellent agreement with fractional differences of  $\approx 0.05\%$  at small scales, and even smaller differences of  $\approx 0.02\%$  on larger scales. The comparison with *Ramses* also shows remarkable agreement with differences of  $0.1\%$  at large scales, with the largest differences of  $\sim 0.7\%$  occurring on small scales by  $z = 0$ . *Cholla* and *Enzo* also show excellent

agreement, with differences of  $< 0.1\%$  at large scales and  $< 0.3\%$  on small scales.

We note that in the version of *Nyx* used in this comparison, a second order scheme was employed to compute the gravitational potential gradient,

$$\frac{\partial \phi_{i,j,k}}{\partial x} = \frac{1}{2\Delta x} (\phi_{i+1,j,k} - \phi_{i-1,j,k}), \quad (40)$$

instead of the fourth-order method described by Equation 19. To have the closest possible comparison, for the *Cholla* simulation used to compare to the *Nyx* results we used Equation 40 to compute the gravitational field. We note that the lower order scheme used to compute the gradient leads to significant differences on the power spectrum at small scales of about 15% relative to the same simulation employing the higher order method.

Additionally, for the comparison with *Enzo* we used the simpler kernel for the Greens function  $G(\mathbf{k}) = -k^{-2}$  in our solver instead of the kernel for the discretized Poisson equation given by Equation 18. The choice of the kernel results in substantial differences, changing the small-scale power spectrum by as much as  $\approx 28\%$  relative to *Enzo* when *Cholla* employs Equation 18.

### 3.3. Adiabatic Cosmological Hydrodynamical Simulation

In §3.1 we showed that *Cholla* accurately solved the gas dynamics in a simplified one dimensional simulation. To test the evolution of the gas in a realistic cosmological evolution, we compared the results of a *Cholla* adiabatic hydrodynamical run to a calculation with *Ram- ses* using identical initial conditions. The configuration for the simulation is the same as the one described in §3.2, but with the addition of an  $\Omega_b = 0.0486$  baryonic component. For the comparison we measure the gas density fluctuation power spectrum directly from the baryon density field in both simulations. Figure 3 shows the results of the comparison, with the power spectrum measured in the *Cholla* simulation (colored lines) shown for several redshifts along with the *Ram- ses* simulation (dashed lines). The bottom panel shows the fractional difference between the *Cholla* and *Ram- ses* power spectrum measurement. On large scales the agreement is excellent ( $\lesssim 1\%$ ), and on smaller scales there are some differences up to a maximum of  $\approx 7\%$  at  $z < 1$ .

As described in §2.3, the dual energy condition used by *Ram- ses* (Equation 15) can suppress shock heating in regions where the gas is converging. This choice can have a significant effect on gas falling into dark matter potential wells, resulting in artificially low gas temperatures. A detailed study of how the dual energy condition affects cosmological gas properties is provided in

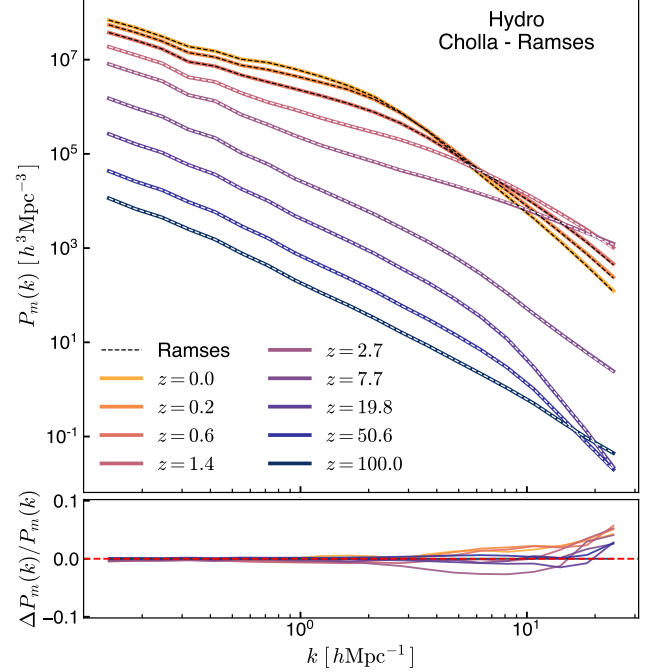


**Figure 3.** Redshift-dependent gas density fluctuation power spectra for an adiabatic cosmological simulation. Shown are the results from our *Cholla* simulation (solid lines) compared with simulation evolved using *Ram- ses* (dashed lines). The bottom panel shows the fractional difference between the *Cholla* and *Ram- ses* power spectra. The agreement is excellent on large scales, and for smaller scales the differences are  $< 7\%$ .

§3.4, but for this power spectrum test we used the *Ram- ses* dual energy condition (Equation 15). We note that the lower gas temperatures computed using the *Ram- ses* dual energy condition result in more power on small scales relative to calculations that use Equation 13. The tests in §3.4 illustrate why we instead use Equation 13 in our CHIPS simulation suite.

Additionally we compared the power spectrum of the gas density fluctuations from a *Cholla* adiabatic cosmological simulation using Equation 13 for the dual energy formalism to an analogous *Enzo* run that evolved the same initial conditions. Figure 4 shows the fractional differences in  $P_m(k)$  resulting from the *Cholla* simulation relative to the *Enzo* run. As shown, the agreement is excellent in the large scales with differences  $< 1\%$  and the smaller scales present differences  $< 15\%$ . From the tests performed we note that the small scale  $P_m(k)$  is highly sensible to the numerical implementation of the hydrodynamics solver and that we are not aware of a robust comparison of the gas  $P_m(k)$  resulting from different codes. We argue that the small differences obtained do not represent an inaccurate evolution of the gas dynamics.

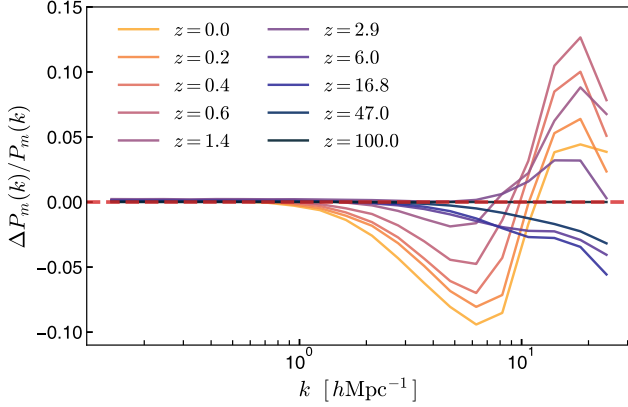


**Figure 4.** Fractional differences in the gas density fluctuation power spectra for an adiabatic cosmological *Cholla* simulation relative to an analogous *Enzo* run, the differences are  $< 1\%$  for large scales and  $< 15\%$  for smaller scales.

### 3.4. Average Cosmic Temperature

In §2.3 we discussed the dual energy formalism used when solving hydrodynamical cosmological simulations. We presented two different approaches for selecting between the advected internal energy  $e$  or the conserved internal energy  $E - v^2/2$ , these two methods are given by Equations 13 and 15 employed by *Enzo* and *Ramses* respectively. To test which approach best captures the shock heating of the infalling gas onto the dark matter halos when implemented in *Cholla*, we measure the mass weighted average gas temperature  $\bar{T}$  in an adiabatic cosmological simulation as described in §3.3, and compare the simulation results to an estimate of the expected gas temperature computed from averaging the virial temperature of collapsed halos with the adiabatically-cooling IGM. We used the ROCKSTAR halo finder (Behroozi et al. 2013) to identify dark matter halos in the *Cholla* simulations, and then computed for each resolved halo a virial temperature as

$$T_{vir} = \frac{m_p}{3k_B} \frac{GM_{vir}}{R_{vir}}. \quad (41)$$

where  $m_p$  is the proton mass,  $k_B$  is the Boltzmann constant, and  $M_{vir}$  and  $R_{vir}$  are the virial mass and radius of the halo measured by ROCKSTAR. To compute our reference estimate of the expected mean cosmic temperature in the simulation, we take the mass in the IGM as simply total gas mass in the simulated box  $M_{total}$  minus the mass in collapsed halos  $M_{halos} = \sum M_{vir}$ . Then, assuming a uniform baryon fraction, the fraction of gas mass present in the IGM is simply  $(M_{total} - M_{halos})/M_{total}$ , and from this we can compute

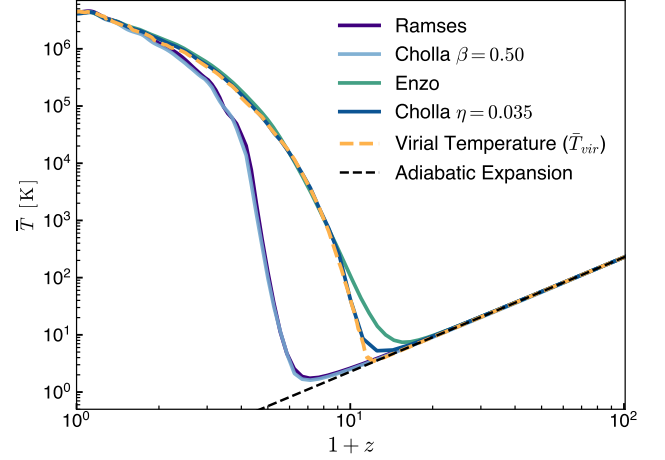


**Figure 5.** Evolution of the mass weighted average cosmic temperature  $\bar{T}$  as a function of redshift for an adiabatic cosmological simulation. Shown as solid lines are the simulation results using *Ramses* (purple), *Enzo* (green), and *Cholla* simulations where Equations 13 (dark blue) or 15 (light blue) were used for the internal energy selection criteria in the dual energy formalism. The dashed lines show estimates of the temperature  $T$  expected from the virial temperature of halos (yellow) and the  $T \propto a^{-2}$  dependence owing to the adiabatic expansion of the universe (black).

the mass weighted average temperature as

$$\bar{T}_{vir} = \sum_{halos} \frac{M_{vir}}{M_{total}} T_{vir} + \left( \frac{M_{total} - M_{halos}}{M_{total}} \right) \left( \frac{a_0}{a} \right)^2 T_0, \quad (42)$$

where the first term corresponds to the mass weighted virial temperature of the gas present in collapsed halos and the second term corresponds to the mass weighted temperature of the gas in the IGM. The IGM temperature is taken to be the initial temperature  $T_0$  scaled by the  $a^{-2}$  factor owing to the adiabatic expansion of the universe.

The results of this comparison are shown in Figure 5, where we plot the mass-weighted average temperature of the gas simulations evolved with *Ramses* (purple line) or *Enzo* (green line). For *Cholla* we ran two simulations with different dual energy conditions, using a criteria similar to *Ramses* (Equation 15, light blue line) or similar to *Enzo* (Equation 13, dark blue line).

All simulations start from the same initial temperature  $T_0 = 230$  K at  $z = 100$ . Afterward, the gas cools as  $T \propto a^{-2}$  owing to universal expansion until the first halos collapse. The temperature of the infalling gas increases owing to shock heating, causing the global average temperature to increase. As Figure 5 shows, the temperature increase happens at roughly two different times for the different simulations. In the *Enzo* calculation and corresponding *Cholla* simulation that uses



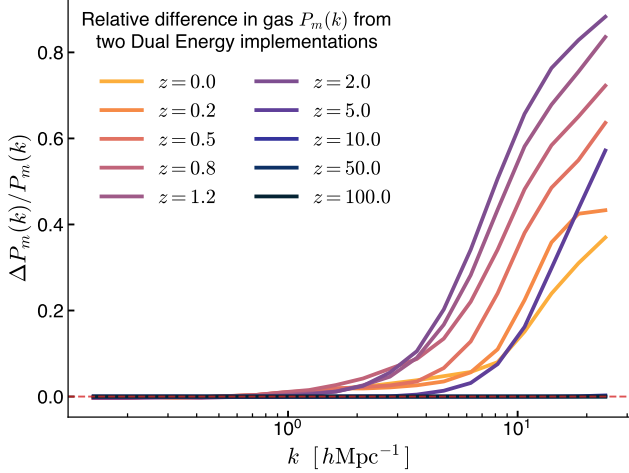


**Figure 6.** Relative fractional difference of gas density fluctuation power spectra in adiabatic cosmological simulations using Equations 13 or 15 for the dual energy implementation. The condition set by Eqn. 15 maintains colder gas for  $1 \lesssim z \lesssim 15$ , resulting in larger power at small scales. The differences range from 30% to 80% at  $0 \lesssim z \lesssim 6$ .

Equation 13 for the dual energy condition, shock heating in the halos becomes significant at  $z \sim 15$  (green and dark blue lines). In the *Ramses* simulation and the *Cholla* calculation using the condition given by Equation 15 (purple and light blue lines), the gas continues cooling owing to expansion until  $z \sim 6$ .

The delayed gas heating in calculations using the dual energy condition given by Eqn. 15 results from the advected internal energy  $e$  being dominantly selected over the conserved internal energy  $E - v^2/2$  for the gas infalling into halos. In this case, the evolution of the advected internal energy  $e$  is given by Equation 5 that does not capture shock heating, and consequently the heating of the gas in the halos is suppressed.

In contrast, if Equation 13 is used for the dual energy condition in the *Cholla* and *Enzo* simulations, the resulting mean cosmic temperature closely follows the virial temperature estimate at  $z < 6$ . We found that for *Cholla*, adopting the parameter value  $\eta = 0.035$  in Equation 13 results in a temperature increase that begins at  $z \approx 12$ , similar to our model estimate.

We note that the mean cosmic gas temperature measured in the *Cholla* adiabatic simulation and our  $\bar{T}_{vir}$  estimate (Eq. 42) computed from the halo properties (Figure 5, dark blue and yellow lines respectively) display a sharp transition at  $z \approx 12$ , when the temperature suddenly increases. We argue that this behavior is a consequence of the limited resolution in our test simulation, as most of the low mass halos that would form at early times ( $z > 12$ ) are not resolved and the heat-

ing of gas during their virialization is not captured. We verify this by computing an estimate of  $\bar{T}_{vir}$  including early, low-mass halos predicted by an analytical mass function (Sheth & Tormen 1999). This analytical estimate shows an earlier and more gradual increase in the mean temperature, starting at  $z \sim 20$ . If instead we limit the minimum halo mass used for the analytical estimate to the minimum resolved halo mass in the test simulations, the estimate follows closely the temperature evolution from the *Cholla* simulation including the sharp increase at  $z \approx 12$ , strongly suggesting that the missing unresolved halos explain the sharp feature in the temperature evolution.

Additionally, we measured the effect on the gas overdensity power spectrum of temperature differences arising from the choice of the dual energy condition. Figure 6 shows the fractional difference of the power spectrum measured in the simulation where Equation 15 was used for the dual energy selection relative to the power spectrum measured in the simulation that instead employed Equation 13. The comparison shows that the power spectrum in the simulation using condition set by Eqn. 15, where the gas remains colder for longer, is  $\sim 50\%$  higher on small scales by  $z \sim 5$ . By  $z \sim 2$  differences on small scales reach  $\sim 80\%$ . Afterward, the two simulations reach similar average temperatures and the differences decrease to  $\sim 30\%$  by  $z = 0$ .

We note that the truncation error  $e_{trunc}$  (Eq. 14) is resolution dependent, and the suppressed shock heating presented in this comparison might be reduced in high resolution AMR simulations. Studying the behavior of condition 15 in such simulations is beyond the scope of this work.

### 3.5. Cosmological Simulation: Chemistry and UV Background

To validate our integration of the chemical network (solved by GRACKLE and advected by the hydrodynamics solver), we ran identical hydrodynamical simulations solved with *Enzo* and *Cholla* following the configuration described in §3.3 but including the non-equilibrium H and He network plus metals in the presence of a spatially-uniform, time-dependent UV background given by the standard HM12 (Haardt & Madau 2012) photoheating and photoionization rates. Figure 7 shows a comparison of projected gas quantities at  $z = 0$  computed by the two codes, with *Cholla* on top and *Enzo* on the bottom. From left to right the panels show projections of dark matter density ( $\rho_{DM}$ ), gas density ( $\rho_b$ ), neutral hydrogen density ( $\rho_{HI}$ ), and gas temperature ( $T$ ). Figure 7 shows qualitatively a remarkable agreement between the results from the two codes.

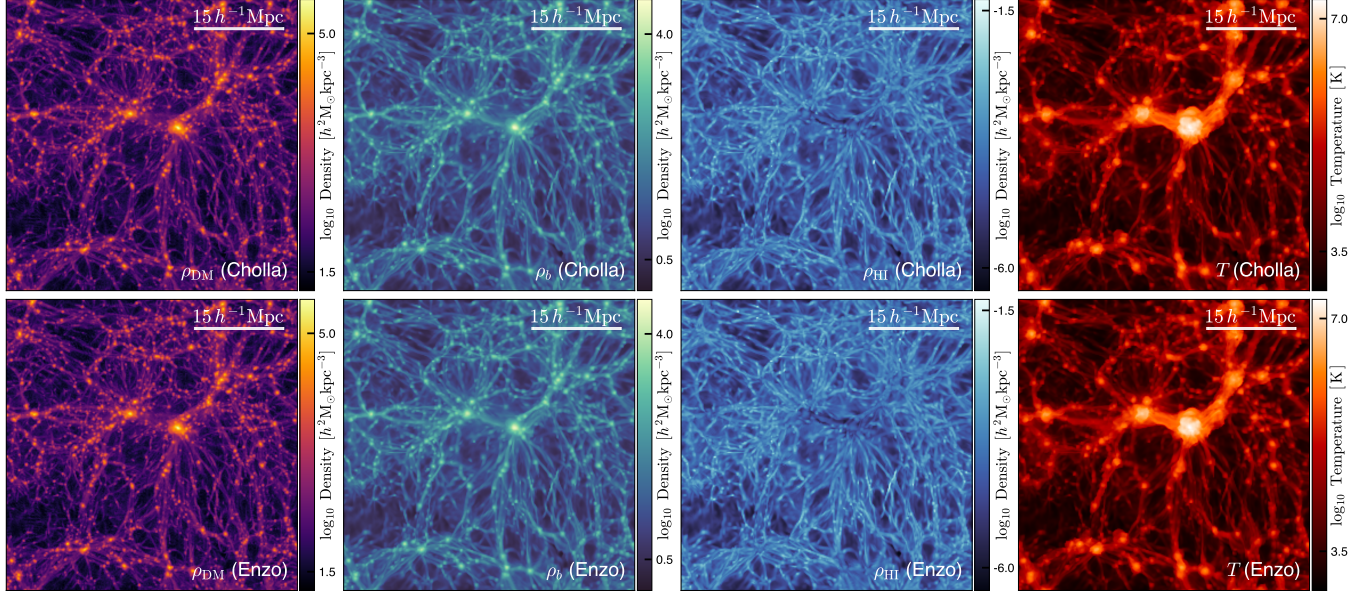


**Figure 7.** Comparison of simulations ( $256^3$  grid and  $L = 50 h^{-1} \text{Mpc}$ ) evolved with *Cholla* (top panels) and *Enzo* (bottom panels). From left to right the columns correspond to projections of dark matter density  $\rho_{\text{DM}}$ , gas density  $\rho_b$ , neutral hydrogen density  $\rho_{\text{HI}}$ , and gas temperature  $T$ , all at redshift  $z = 0$ .

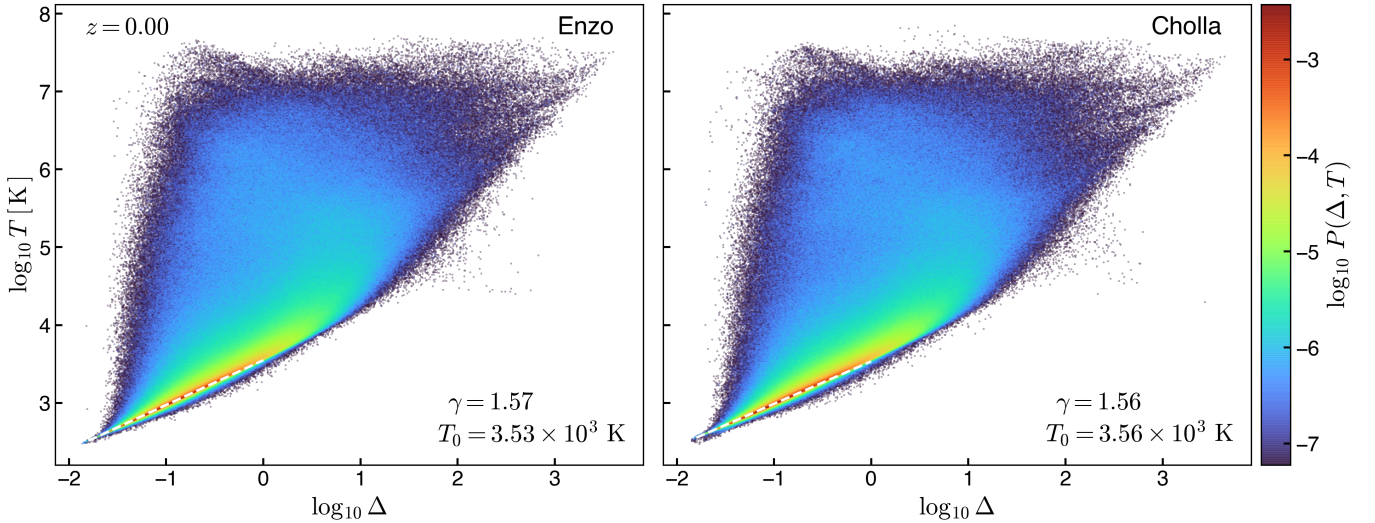


**Figure 8.** Comparison of the density-temperature ( $\Delta = \rho_b / \bar{\rho}_b$ ) distribution at redshift  $z = 0$  for analogous simulations ( $256^3$  grid and  $L = 50 h^{-1} \text{Mpc}$ ) evolved with *Enzo* (left) and *Cholla* (right) using the HM12 photoheating and photoionization rates. The distribution of the gas in both simulations is remarkably similar and the differences for the parameters  $T_0$  and  $\gamma$  are  $< 1\%$ , demonstrating an excellent agreement for the gas distribution in the IGM between the codes. (The parameters  $T_0$  and  $\gamma$  are defined in §5.)

For a more detailed comparison, we measured the density-temperature distribution from both simulations. Figure 8 shows the results from the *Enzo* (left) and *Cholla* (right) runs at  $z = 0$ . As shown, the distribution of the gas in the simulations is remarkably similar. Additionally the parameters  $T_0$  and  $\gamma$  which model the distribution of the diffuse gas in the IGM (see §5

for details) differ by less than 1% showing an excellent agreement between these simulations.

#### 4. SIMULATION SUITE

In this section we present the CHIPS (**CHolla IGM Photoheating Simulations**) simulation suite, a set of high resolution simulations performed using the newly extended version of the *Cholla* code described above.



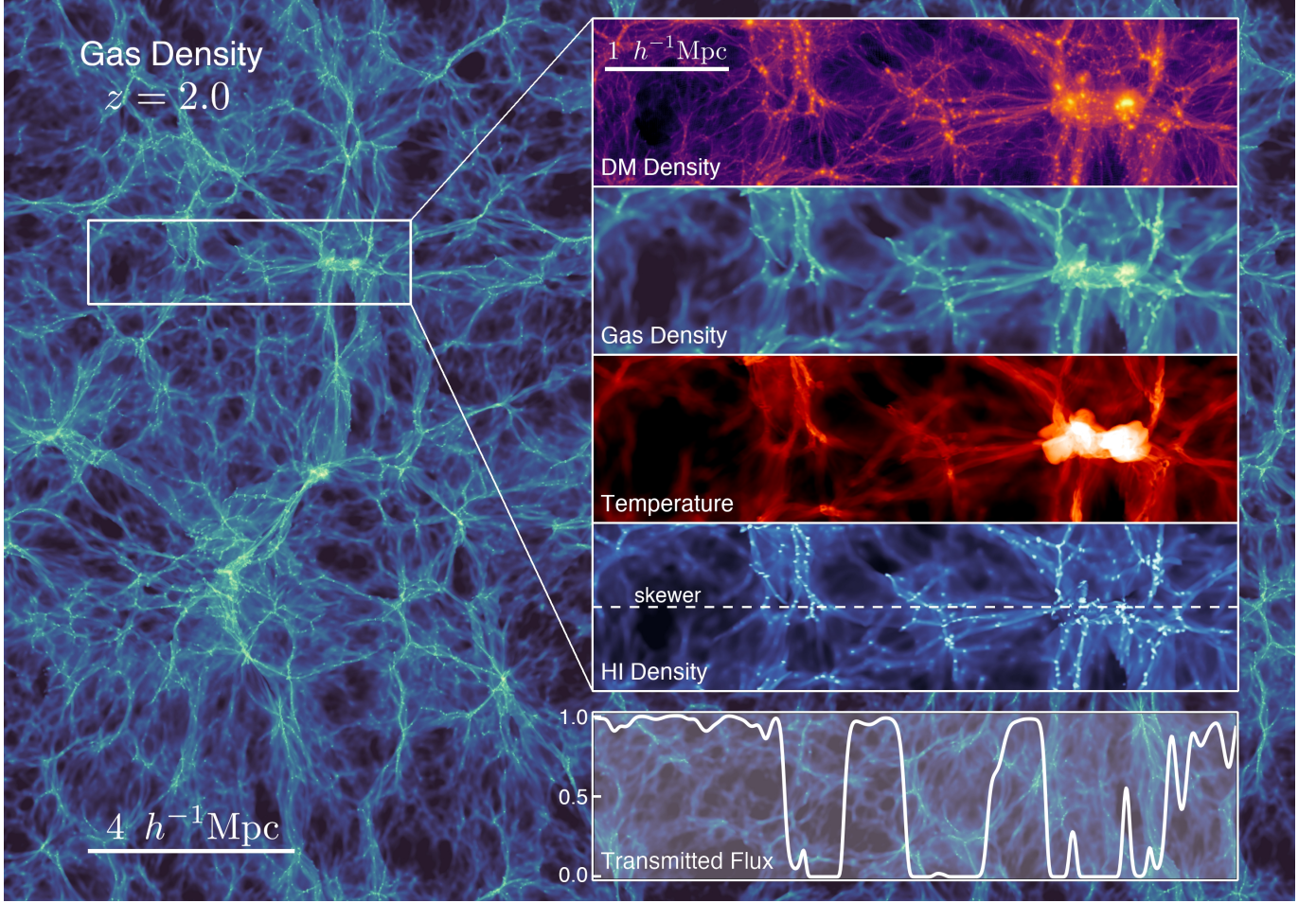


**Figure 9.** Projection of the gas density at redshift  $z = 2$  from the CHIPS.P19 simulation ( $2048^3$  grid,  $L = 50 h^{-1}\text{Mpc}$ , and  $1.5 h^{-1}\text{Mpc}$  projected). The zoom-in region shows the dark matter density  $\rho_{\text{DM}}$ , gas density  $\rho_b$ , gas temperature  $T$ , and neutral hydrogen density  $\rho_{\text{HI}}$  from top to bottom. A skewer crossing the center of the zoom-in region is marked over the neutral hydrogen distribution, and the Lyman- $\alpha$  transmitted flux along the skewer is shown in the bottom panel. The scale labels refer to proper distances.

The suite consists of a series of simulations run with a fiducial resolution of  $N = 2048^3$  cells, varying the cosmic photoheating and photoionization rates from evolving UV background radiation fields and with a range of cosmological parameters. All the CHIPS simulations evolve a primordial gas composition ( $X = 0.76$ ,  $Y = 0.24$ ), without the inclusion of metal line cooling as star formation is not accounted for in the simulations.

Table 1 details the properties of our initial CHIPS simulations. The primary simulations for our initial analysis of the Lyman- $\alpha$  forest are CHIPS.HM12 and CHIPS.P19, which use the Planck Collaboration et al. (2018) cosmological parameters and the Haardt & Madau (2012) and Puchwein et al. (2019) photoionization and photoheating rates, respectively, in an  $L = 50 h^{-1}\text{Mpc}$  box. The Puchwein et al. (2019) model adopts the most recent determinations of the ionizing emissivity due to stars and AGN, as well as of the

H I absorber column density distribution. Another major improvement is a new treatment of the IGM opacity for ionizing radiation that is able to consistently capture the transition from a neutral to ionized IGM. For these fiducial runs, we output 150 snapshots over the redshift range  $z = [16, 2]$ , spacing the time between snapshots at  $\Delta a = 1.83 \times 10^{-3}$  intervals. In each snapshot, we record the conserved fluid quantities ( $\rho$ ,  $\rho v_x$ ,  $\rho v_y$ ,  $\rho v_z$ ,  $E$ ), the gas internal energy  $u$ , the neutral hydrogen H I, neutral helium He I, singly-ionized helium He II, and electron  $n_e$  densities, and the gravitational potential  $\phi$  on the simulation grid. We also record all the dark matter particle positions and velocities. The detailed analyses performed on the simulation outputs are described in §5.

We complement the fiducial models with four additional simulations (CHIPS.P19.[A1-A4]) that use the Puchwein et al. (2019) photoionization and photoheat-

**Table 1.** CHIPS Simulation Suite

Simulation	Resolution	Box Size $L$ [ $h^{-1}\text{Mpc}$ ]	Parameters $[h, \Omega_m, \Omega_b, \sigma_8, n_s]$	UV Background
CHIPS.HM12	$N = 2048^3$	50	[0.6766, 0.3111, 0.0497, 0.8102, 0.9665]	Haardt & Madau (2012)
CHIPS.P19	$N = 2048^3$	50	[0.6766, 0.3111, 0.0497, 0.8102, 0.9665]	Puchwein et al. (2019)
Alternative Cosmologies				
CHIPS.P19.A1	$N = 2048^3$	50	[0.6835, 0.3010, 0.0484, 0.8098, 0.9722]	Puchwein et al. (2019)
CHIPS.P19.A2	$N = 2048^3$	50	[0.6917, 0.2905, 0.0477, 0.8052, 0.9783]	Puchwein et al. (2019)
CHIPS.P19.A3	$N = 2048^3$	50	[0.7001, 0.2808, 0.0470, 0.8020, 0.9846]	Puchwein et al. (2019)
CHIPS.P19.A4	$N = 2048^3$	50	[0.7069, 0.2730, 0.0465, 0.7997, 0.9896]	Puchwein et al. (2019)
Resolution Studies				
CHIPS.P19.R1	$N = 1024^3$	50	[0.6766, 0.3111, 0.0497, 0.8102, 0.9665]	Puchwein et al. (2019)
CHIPS.P19.R2	$N = 512^3$	50	[0.6766, 0.3111, 0.0497, 0.8102, 0.9665]	Puchwein et al. (2019)

NOTE—Resolution refers to the number of both grid cells and dark matter particles.

ing rates but vary the cosmological parameters  $h$ ,  $\Omega_m$ ,  $\Omega_b$ ,  $\sigma_8$ , and  $n_s$  within the uncertainties reported by Planck Collaboration et al. (2018). For each simulation, a flat cosmology is assumed and we set  $\Omega_\Lambda = 1 - \Omega_m$ .

Table 1 also lists properties of the additional  $N = 1024^3$  (CHIPS.P19.R1) and  $N = 512^3$  (CHIPS.P19.R2) simulations used in our resolution study to demonstrate the numerical convergence of our results (see Appendix A).

The CHIPS simulation suite was run on the Summit system (Oak Ridge Leadership Computing Facility at the Oak Ridge National Laboratory), each of the  $2048^3$  simulations ran in 512 GPUs for  $\sim 11$  hours costing  $\sim 1000$  node-hours. As described in §2.9, the slowest component of the simulation is the GRACKLE update step, consuming about half of the computational time for these runs. This motivates the ongoing development of a H+He network solver implemented to run in the GPUs which will potentially reduce this bottleneck. The subsequent analysis of the simulation output data was performed using the *lux* supercomputer at UC Santa Cruz.

## 5. EVOLUTION OF THE IGM FOR TWO PHOTOHEATING HISTORIES

Redshift-dependent photoionization and photoheating rates of intergalactic gas substantially affect IGM properties. By comparing the CHIPS.HM12 with the CHIPS.P19 simulation, we can learn about how detailed differences in photoheating history lead to observable differences in the Lyman- $\alpha$  forest and potentially discriminate between them by further comparisons with data. We first compare the thermal history of the diffuse IGM between the simulations (§5.1). The redshift-

dependent thermal properties of the IGM in the models provide a context for interpreting measurements of the simulated forest. We discuss our methods for generating mock Lyman- $\alpha$  absorption spectra in §5.2. These simulated spectra then provide estimates of the Lyman- $\alpha$  forest optical depth (§5.3) and transmitted flux power spectra (§5.4).

### 5.1. Thermal History of the Diffuse IGM

The gas in the diffuse IGM comprises most of the baryons in the universe and follows a well defined density-temperature power-law relation (Hui & Gnedin 1997; McQuinn 2016; Puchwein et al. 2015) given by

$$T(\Delta) = T_0 \Delta^{\gamma-1}, \quad (43)$$

where  $\Delta = \rho_b / \bar{\rho}_b$  is the gas overdensity,  $T_0$  is the temperature at the mean cosmic density  $\bar{\rho}_b$ , and  $\gamma - 1$  corresponds to the power-law index of the relation. The time evolution of the parameters  $T_0$  and  $\gamma$  is determined by the photoheating from to hydrogen and helium ionization, cooling owing to the expansion of the universe, and inverse Compton cooling, recombination, and collisional processes.

Figure 10 shows the density-temperature distribution of the gas in our simulations at redshift  $z = 5$ , with CHIPS.HM12 shown on the left and CHIPS.P19 shown on the right. The distributions resulting from the two UVB models are similar for gas collapsed into resolved structures ( $\Delta > 10$ ), but for low density gas ( $\Delta < 10$ ) the temperatures in the HM12 model are significantly lower owing to the earlier completion of hydrogen reionization ( $z \sim 13$ ). The gas temperature in this model has had subsequently more time to decrease owing to cooling processes and adiabatic expansion. For the P19



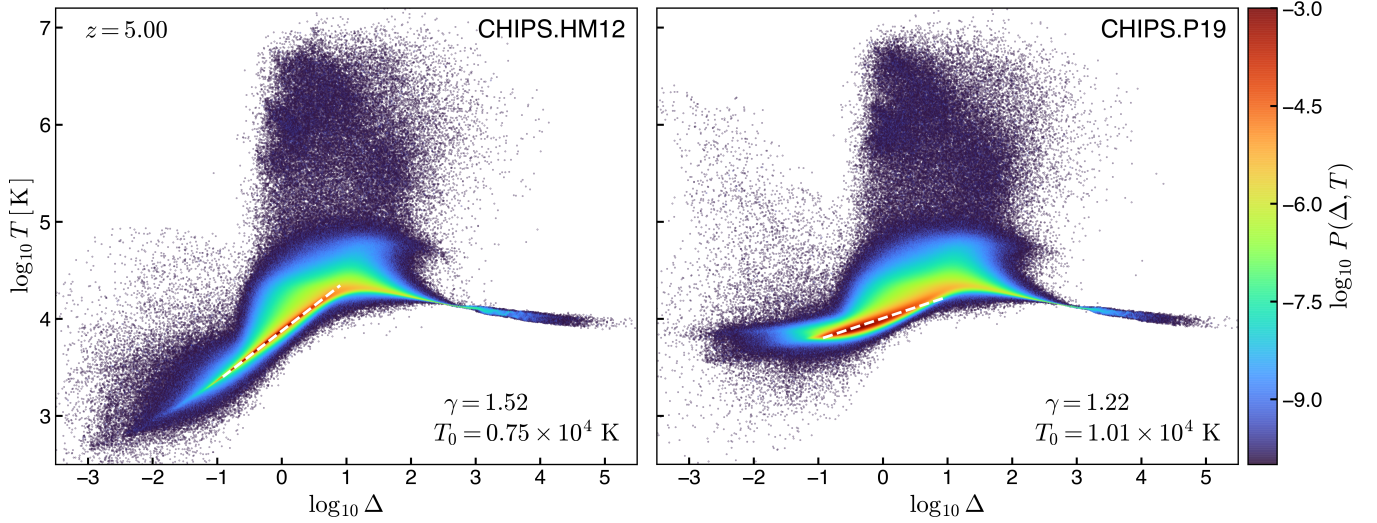


**Figure 10.** Volume-weighted density-temperature distribution of gas at redshift  $z = 5$  in our two fiducial simulations (CHIPS.HM12, left; CHIPS.P19, right). The low density gas ( $\Delta < 10$ ) is colder for the [Haardt & Madau \(2012\)](#) model owing to H reionization ending earlier. Dashed lines show the best fit power-law  $\Delta$ - $T$  relation for the parameters  $T_0$  and  $\gamma$ .

model, where reionization ends at  $z \sim 6$ , there has been less time to cool by  $z = 5$ , resulting in a higher  $T_0$  and lower  $\gamma$  at this epoch.

For each snapshot of the simulation, we determined the parameters  $T_0$  and  $\gamma$  by fitting Equation 43 to the low density ( $-1 < \log_{10} \Delta < 1$ ) region of the density-temperature distribution. We divided the selected interval into fifty equal bins in  $\log_{10}(\Delta)$ , and for each bin  $i$  the maximum of the marginal temperature distribution  $P(T|\Delta_i)$  and the temperature range containing the 68% highest probability density was used to define the bin temperature  $T_i$  and its corresponding uncertainty  $\delta T_i$ . The coordinates  $(\Delta_i, T_i)$  and uncertainty values  $\delta T_i$  were used as input to a Monte Carlo Markov Chain that sampled the parameters  $T_0$  and  $\gamma$ , initialized from uniform prior distributions, and returned posterior distributions for the thermal parameters that best match the density-temperature relation measured from the simulations. From the posterior distributions we extracted best-fit values for  $T_0$  and  $\gamma$  and corresponding parameter uncertainties  $\delta T_0$  and  $\delta \gamma$ .

The redshift evolution of the parameters  $T_0$  and  $\gamma$  for the two UVB models is shown in Figure 11, where the effects of the two ionization histories on the thermal structure of the diffuse IGM are illustrated. The evolution of the IGM follows several phases. First, before H I reionization is complete, the photoheating owing to hydrogen ionization increases the temperature to an early local maximum. After all the H I is ionized, the diffuse IGM cools by adiabatic expansion and inverse Compton cooling until the onset of He II reionization reheats the IGM

to a global maximum. Once He II is fully ionized, the IGM again cools adiabatically to the present day.

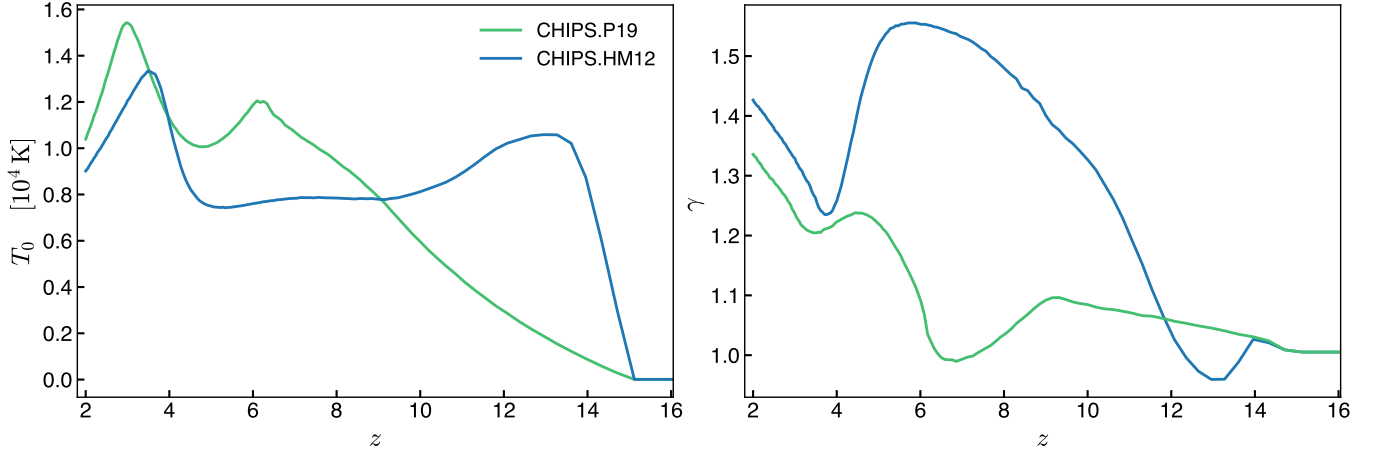
The HM12 UVB (blue line) causes a quick H I reionization around redshift  $z \sim 14$  and cools afterward. In the interval between  $z \sim 6 - 10$ , the temperature at mean density  $T_0$  plateaus at  $T \sim 8 \times 10^3$  K while underdensities ( $\Delta < 1$ ) keep cooling, mostly due to adiabatic expansion, this results in an increasing  $\gamma$  until  $z \sim 5$ .

For  $z \leq 15$  the ionization rates for the late-reionization P19 model are significantly lower until  $z \sim 6.5$ , resulting in a gradual heating of the IGM. The IGM remains close to isothermal ( $\gamma \sim 1$ ) until H I reionization completes at  $z \sim 6.2$ . Intergalactic gas then cools just for short period before He II reheating, resulting in a higher  $T_0$  than in the HM12 model.

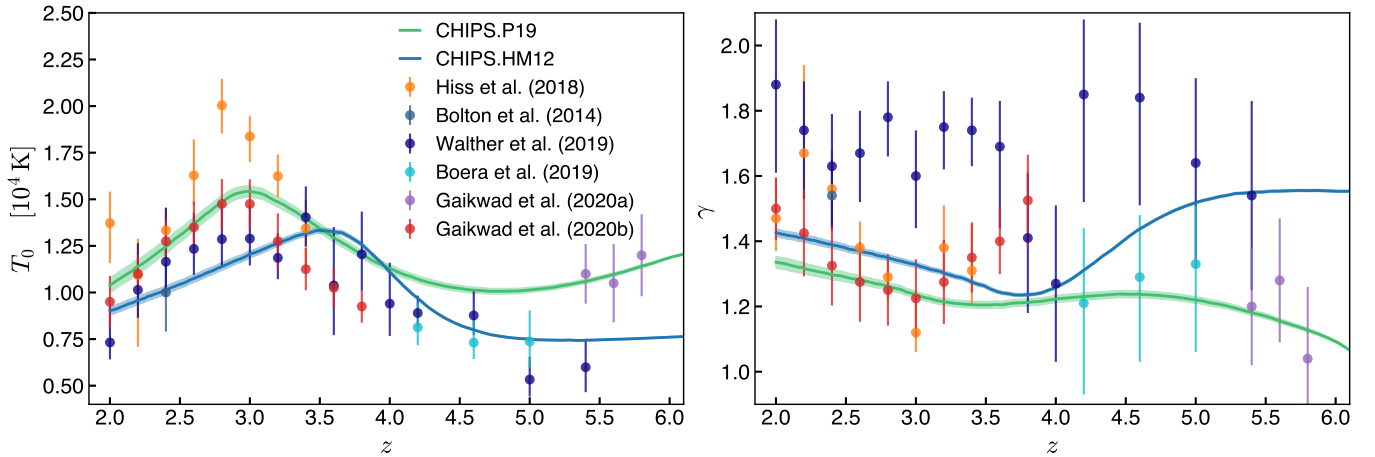
While in both runs helium reheating starts around  $z \sim 4.5$ , the reionization of He II is completed earlier in CHIPS.HM12. At  $z < 3$ , the residual heating from photoionization of recombining atoms is inefficient, and the IGM continues to cool all the way down to  $z = 0$ , decreasing  $T_0$  and increasing  $\gamma$ .

Figure 12 shows a comparison between the thermal parameters  $T_0(z)$  and  $\gamma(z)$  from our simulations and previous observational inferences ([Bolton et al. 2014](#); [Hiss et al. 2018](#); [Boera et al. 2019](#); [Walther et al. 2019](#); [Gaikwad et al. 2020b,a](#)). The shaded regions correspond to the uncertainty in  $T_0$  and  $\gamma$  resulting from our power-law fitting procedure. For the observations, the values of  $T_0$  and  $\gamma$  are determined in different ways.

[Walther et al. \(2019\)](#) and [Boera et al. \(2019\)](#) both follow a similar approach by generating Lyman- $\alpha$  flux power spectra from simulations evolved with different



**Figure 11.** Redshift evolution of the gas temperature  $T_0$  at mean density and the index  $\gamma$  of the density-temperature relation. Shown are results from our reference simulations CHIPS.HM12 (blue lines) and CHIPS.P19 (green lines). H I reionization ends earlier ( $z \sim 13$ ) for the HM12 model, compared with  $z \sim 6$  for the P19 model, allowing more time for the low density gas to cool. He II reionization begins at  $z \sim 4.5$  in both models, but the lower He II photoionization rates for the P19 model result in He II being fully ionized at a later time ( $z \sim 3$ ) compared with  $z \sim 3.8$  for the HM12 run.



**Figure 12.** Redshift evolution of the density-temperature parameters  $T_0$  and  $\gamma$  from the CHIPS.HM12 (blue) and CHIPS.P19 (green) simulations. The shaded regions show the uncertainty resulting from the power-law fitting procedure. Points show the observational results from Hiss et al. (2018), Bolton et al. (2014), Walther et al. (2019), Boera et al. (2019), Gaikwad et al. (2020b), and Gaikwad et al. (2020a).

thermal histories, resulting in multiple trajectories of  $T_0$  and  $\gamma$ . For each simulation snapshot, they determine the best fit  $T_0$ ,  $\gamma$ , and mean transmitted flux  $\bar{F}$  by performing Bayesian inference comparing the generated flux power spectra from the different simulations to observations.

Hiss et al. (2018) and Bolton et al. (2014) measure the  $b$ - $N_{\text{HI}}$  distribution obtained from decomposing the Lyman- $\alpha$  forest spectra into a collection of Voigt profiles, and then infer thermal parameters by matching the  $b$ - $N_{\text{HI}}$  distribution from their simulations to the observed distribution. Gaikwad et al. (2020a) follows an analogous approach by comparing simulation results to Voigt

profiles fitted to transmission spikes in the inverse transmitted flux  $1 - F$  in  $z > 5$  spectra. In a recent analysis, Gaikwad et al. (2020b) report more precise results by inferring  $T_0$  and  $\gamma$  from combined constraints obtained through a comparison between simulated and observed Lyman- $\alpha$  forest flux power spectra,  $b$ - $N_{\text{HI}}$  distributions, wavelet statistics, and curvature statistics.

During the epoch of He II reionization and afterward, Hiss et al. (2018) infer a peak in  $T_0$  ( $z \sim 2.8$ ) that is significantly higher than the results from all the other analysis, while the measurements from Gaikwad et al. (2020b) are mostly higher than those obtained by Walther et al. (2019) and Bolton et al. (2014) their

results still are consistent within  $1\sigma$  of each other. Compared to the simulations, both the P19 and HM12 models result in a increase of  $T_0$  due to He II photoheating that begins too early ( $z \sim 4.2$ ) to be consistent with the measurements from Gaikwad et al. (2020b) and Walther et al. (2019) simultaneously. The heating from He II reionization could be delayed in the P19 model by decreasing the He II photoheating and photoionization rates, effectively also slightly decreasing the peak of  $T_0$  at  $z \sim 2.8$ , this would produce a trajectory for  $T_0$  at  $z \lesssim 4$  that better matches the results from Gaikwad et al. (2020b) and Walther et al. (2019).

For  $z > 4$ , the results from Walther et al. (2019) and Boera et al. (2019) measure temperatures lower than those produced by the Puchwein et al. (2019) model. In particular, at  $z \geq 5$  Walther et al. (2019) find remarkably low temperatures, which may be related to the strong correlation between  $T_0$  and  $\bar{F}$  in their analysis.

The  $\gamma$  values inferred by Walther et al. (2019) are overall higher than all the other data sets. In the redshift range  $2.6 \lesssim z \leq 5$ , both our CHIPS.HM12 and CHIPS.P19 simulations produce  $\gamma(z)$  consistent with the measurements from Hiss et al. (2018) and Boera et al. (2019), within their respective uncertainties. Additionally both models result in  $\gamma(z)$  consistent with the results from Gaikwad et al. (2020b) only for  $z \lesssim 3.3$  as their observational inference results in higher values ( $\gamma \sim 1.5$ ) at  $z \sim 3.8$  compared to  $\gamma \sim 1.3$  produced in both simulations at this redshift. Delaying the heating from He II reionization would allow more time for the diffuse gas to cool after H I reionization, effectively increasing  $\gamma$  produced by the models at  $z \sim 4$ , to be in better agreement with the results from Gaikwad et al. (2020b).

The CHIPS.P19 results are consistent with constraints on  $T_0$  and  $\gamma$  for  $z > 5.3$  from Gaikwad et al. (2020a), likely because H I reionization ends at  $z \sim 6$  in the Puchwein et al. (2019) photoionization and photoheating model. Although, reconciling the high  $\gamma \sim 1.5$  at  $z \sim 3.8$  from Gaikwad et al. (2020b) with the low  $\gamma \sim 1.2$  at  $z \sim 5.5$  inferred by Gaikwad et al. (2020a) could require the low density gas to cool faster than physically possible in a spatially-uniform UV background model. However, near H I reionization a non-uniform UV background may be required for the simulations to model accurately the effects of a “patchy” reionization (Keating et al. 2020).

## 5.2. Synthetic Lyman- $\alpha$ Forest Spectra

The Lyman- $\alpha$  forest is a sensitive probe of the diffuse baryons in the IGM, as the amplitude and width of the

absorption lines in the forest trace the neutral hydrogen density and the gas temperature. The observed Lyman- $\alpha$  forest global statistics, such as the effective optical depth and the transmitted flux power spectra, constrain the thermal state of the IGM. To compare directly with the observed effective optical depth and the transmitted flux power spectra, we compute synthetic Lyman- $\alpha$  forest spectra from our high resolution simulations. In total we drew 60000 skewers through the simulation volume, located in random positions and aligned parallel with the three box axes (20000 skewers for each axis). Along each skewer, the neutral hydrogen density, gas temperature, and the component of the velocity parallel to the line of sight are sampled at the native resolution of the simulation, rendering 2048 uniformly distributed pixels for each skewer. The optical depth as a function of frequency  $\tau_\nu$  along the skewer is computed by integrating the Lyman- $\alpha$  interaction cross section  $\sigma_\nu$  and the neutral hydrogen number density  $n_{\text{HI}}$  along the line of sight, following

$$\tau_\nu = \int n_{\text{HI}} \sigma_\nu dr, \quad (44)$$

where  $dr$  is the physical length of the path element. Assuming a Doppler profile for the absorption line, the optical depth at frequency  $\nu_0$  is given by

$$\tau_{\nu_0} = \frac{\pi e^2}{m_e c} f_{12} \int \frac{n_{\text{HI}}}{\sqrt{\pi} \Delta \nu_D} \exp \left[ - \left( \frac{\nu - \nu_0}{\Delta \nu_D} \right)^2 \right] dr, \quad (45)$$

where  $f_{12}$  is the Lyman- $\alpha$  transition upward oscillator strength,  $\Delta \nu_D = (b/c)\nu_0$  is the absorption width owing to Doppler shifts and  $b = \sqrt{2k_B T/m_H}$  corresponds to the thermal velocity of the gas. The shift in the frequency of absorption along the skewer is given by the Doppler shift from the change in the gas velocity along the line of sight,

$$\nu = \nu_0 \left( 1 - \frac{u - u_0}{c} \right). \quad (46)$$

Applying a variable transformation from frequency to velocity space and the expansion relation  $du = Hdr$ , the optical depth as a function of velocity is expressed as

$$\tau_{u_0} = \frac{\pi e^2 \lambda_0}{m_e c H} f_{12} \int \frac{n_{\text{HI}}}{\sqrt{\pi} b} \exp \left[ - \left( \frac{u - u_0}{b} \right)^2 \right] du. \quad (47)$$

Following the method described by Lukić et al. (2015), we solved the Gaussian integral analytically and computed the optical depth along the discretized line of sight using

$$\tau_j = \frac{\pi e^2 \lambda_0 f_{12}}{m_e c H} \sum_i \frac{1}{2} n_{\text{HI},i} \left[ \text{erf} \left( y_{j+1/2,i} \right) - \text{erf} \left( y_{j-1/2,i} \right) \right], \quad (48)$$

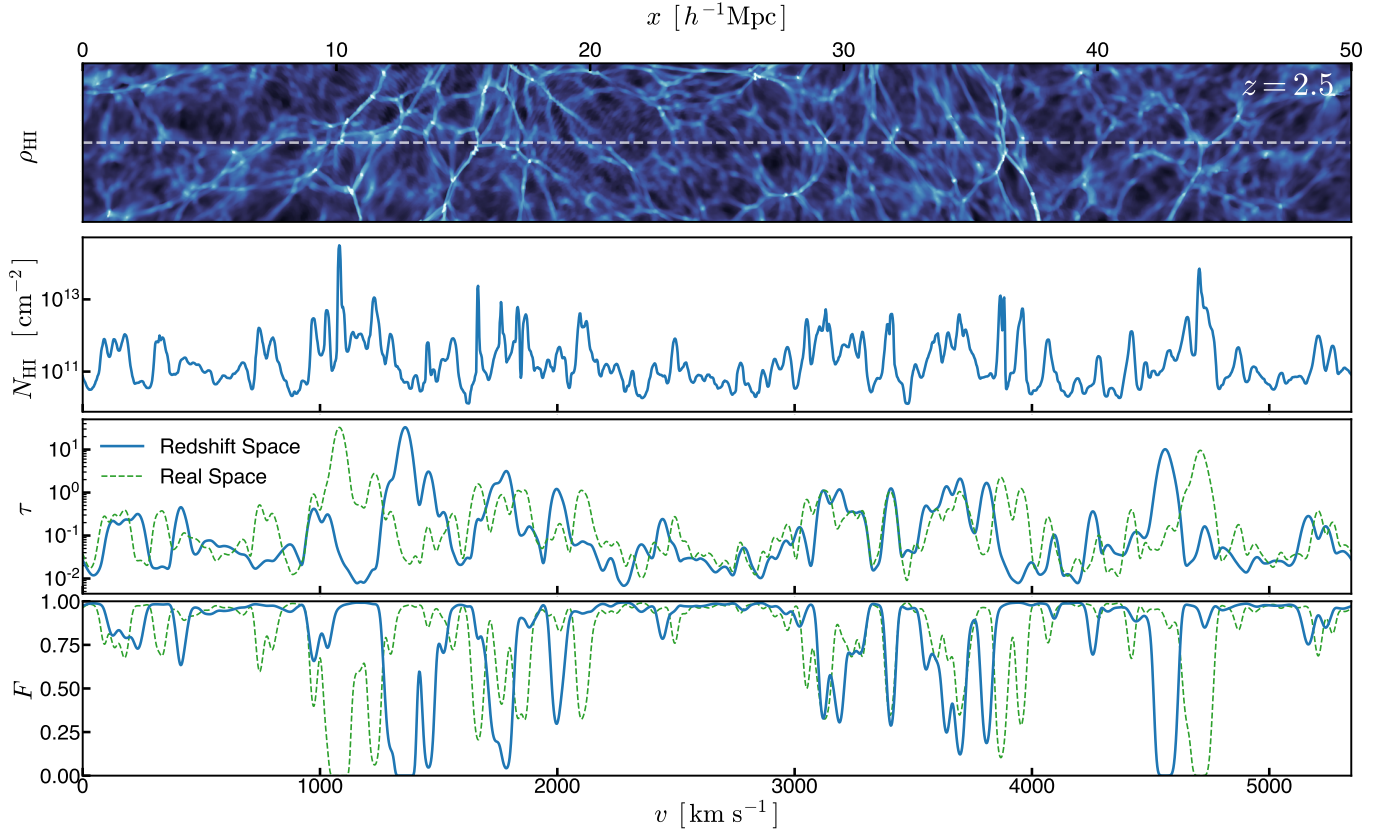


**Figure 13.** Elements for the calculation of the transmitted flux along a single skewer crossing the CHIPS.P19 simulation box at redshift  $z = 2.5$ . Shown in the panels from top to bottom are the neutral hydrogen density  $\rho_{\text{HI}}$  in a region surrounding the skewer, neutral hydrogen column density  $N_{\text{HI}}$  along the skewer, optical depth  $\tau$  computed via Equation 48, and transmitted flux  $F = \exp(-\tau)$  along the line of sight.

where the argument to the error function is

$$y_{j\pm 1/2,i} = (v_{\text{H},j\pm 1/2} - v_{\text{H},i} - v_{\text{LOS},i}) / b_i. \quad (49)$$

The term  $v_{\text{H},j\pm 1/2}$  corresponds to the Hubble flow velocity at the interfaces of cell  $j$  and the terms  $v_{\text{H},i}$  and  $v_{\text{LOS},i}$  represent the centered values of Hubble velocity and the line of sight component of the peculiar velocity of the gas at cell  $i$ . Note that the factor of  $1/2$  in Equation 48 comes from the definition used for the error function,  $\text{erf}(x) = 1/\sqrt{\pi} \int_{-x}^x \exp(-t^2) dt$ .

The calculation of the optical depth  $\tau$  and the transmitted flux for a single skewer spanning across the length of the CHIPS.P19 box at redshift  $z = 2.5$  is illustrated in Figure 13. The figure panels from top to bottom show the distribution of the neutral hydrogen density in the neighborhood of the skewer ( $\rho_{\text{HI}}$ ), the 1D neutral hydrogen column density integrated over the length of the cell across the skewer ( $N_{\text{HI}}$ ), the optical depth  $\tau$  in redshift space computed via Equation 48 (blue line) and ignoring the shift of the absorption lines due to peculiar real space velocities (green), and the transmitted flux  $F = \exp(-\tau)$  along the skewer in both redshift (blue) and real (green) space.

### 5.3. Evolution of the Lyman- $\alpha$ Effective Optical Depth

The Lyman- $\alpha$  effective optical depth  $\tau_{\text{eff}}$  is a measure of the overall H I content of the gas in the IGM. Hence,  $\tau_{\text{eff}}$  tracks the ionization state of hydrogen and the intensity of the ionizing UV background. To compare with observational measurements of  $\tau_{\text{eff}}$ , we computed synthetic Lyman- $\alpha$  absorption spectra from all the outputs of our two simulations using the method described in §5.2. From the large sample of skewers, the effective optical depth is computed as  $\tau_{\text{eff}} = -\log(\bar{F})$ , where  $\bar{F}$  is the transmitted flux averaged over all skewers.

The redshift evolution of the effective optical depth  $\tau_{\text{eff}}$  for our two simulations is shown as colored lines in Figure 14 (blue and green for the HM12 and P19 models, respectively) and the shaded region shows the variability of  $\tau_{\text{eff}}$  measured over the different skewers. For each redshift the shaded interval corresponds to the optical depth computed from the highest probability interval that encloses 68% of the distribution of the transmitted flux averaged over individual skewers.

The effective optical depth resulting from the HM12 UVB model (blue) shows good agreement with the ob-



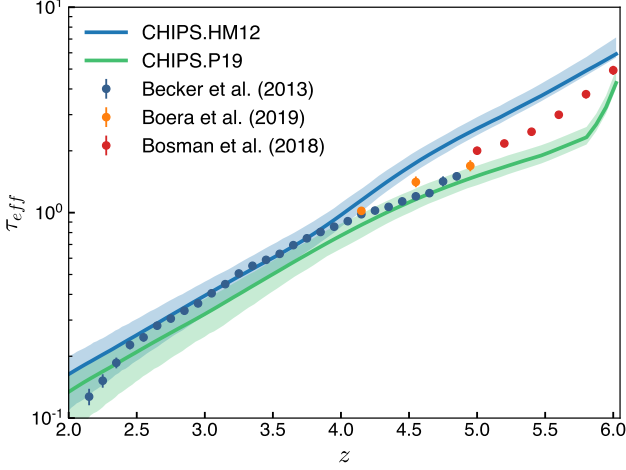


**Figure 14.** Redshift evolution of the effective optical depth  $\tau_{eff}$ . Shown are our simulated measurements from CHIPS.HM12 (blue) and CHIPS.P19 (green), compared to data from Becker et al. (2013), Boera et al. (2019) and Bosman et al. (2018) (data points). Measurements of  $\tau_{eff}$  from the HM12 model match the observations at  $2.5 \lesssim z \lesssim 4.2$ , but display higher amounts of H I for  $z \gtrsim 4.2$  owing to the low temperatures at those redshifts. The P19 model produces values of  $\tau_{eff}$  slightly lower than the observations for  $2.5 \lesssim z \lesssim 4$ , suggesting that He II reionization is overheating the IGM at these epochs. For  $5 < z < 5.8$  the P19 model results in measurements of  $\tau_{eff}$  significantly lower than the observations. This discrepancy could result from the relatively hot IGM produced by the P19 model at this epoch and may be addressed by introducing a non-uniform UVB in the simulations.

served data (Becker et al. 2013) for  $z < 4$ , but underestimates the ionization fraction at  $z > 4$ . At the higher redshifts, the model produces an excess of neutral hydrogen, likely because the early H I reionization renders the gas too cold, this results in an effective optical depth higher than estimated by Boera et al. (2019) and measured by Bosman et al. (2018).

The P19 model (green) has too high an ionization fraction, resulting in an optical depth that is slightly lower than the observations. In the redshift range  $2.5 \lesssim z \lesssim 4$ , He II reionization in the P19 model is overheating the IGM. For  $5 < z < 5.8$ , the P19 model produces  $\tau_{eff}$  that are 10 to 25% lower than the observations, suggesting that the temperatures of the IGM in this model at  $z \sim 5.2$  are higher than those in reality. At these high redshifts ( $z \gtrsim 5.4$ ), a non-uniform UV background may be required to accurately represent the effects of a “patchy” reionization in  $\tau_{eff}$  (Keating et al. 2020), and the inclusion of a non-uniform UVB could reduce the discrepancies between the data and the P19 model at these times.

#### 5.4. Lyman- $\alpha$ Transmitted Flux Power Spectrum

On scales of a few Mpc, the Lyman- $\alpha$  flux power spectrum (FPS) is an excellent probe of the thermal properties of the photoionized IGM and can constrain the IGM temperature at various epochs. On scales below  $\sim 100$  kpc, the FPS exhibits a cutoff beyond which the Lyman- $\alpha$  forest has suppressed structure owing to both the pressure smoothing of the gas distribution (which sets the pressure smoothing scale  $\lambda_P$ ) as well as the thermal Doppler broadening of the absorption lines. To compare the FPS produced by the UVB models in the simulations with observation, we measured the Lyman- $\alpha$  transmitted flux power spectra from the large sample of skewers computed as described in §5.2. The FPS as a function of velocity  $u$  is obtained from the flux fluctuations as

$$\delta_F(u) \equiv \frac{F(u) - \bar{F}}{\bar{F}}, \quad (50)$$

where  $F(u)$  is the transmitted flux along the skewer over the velocity interval  $[0, u_{max}]$  and  $\bar{F} = \exp(-\tau_{eff})$  is the transmitted flux averaged over all the skewers. The FPS is commonly expressed in terms of the dimensionless quantity  $\Delta_F^2$ , defined as

$$\Delta_F^2(k) = \frac{1}{\pi} k P(k). \quad (51)$$

The transmitted flux power spectrum  $P(k)$  is computed as

$$P(k) = u_{max} \left\langle \left| \tilde{\delta}_F(k) \right|^2 \right\rangle \quad (52)$$

$$\tilde{\delta}_F(k) = \frac{1}{u_{max}} \int_0^{u_{max}} e^{-iku} \delta_F(u) du, \quad (53)$$

where  $k = 2\pi/u$  corresponds to the wavenumber associated to the velocity  $u$  and has units of  $\text{s km}^{-1}$  and  $u_{max}$  is the Hubble flow velocity for the box length  $u_{max} = HL/(1+z)$ . From our simulations, we measured the FPS resulting from both UVB models and compared with the analogous observational measurements. Our results are shown in Figures 15 and 16, where the lines show the FPS averaged over all the skewers and the shaded bars show the  $\sigma(k)/\sqrt{N_{ind}(k)}$  region. Here  $\sigma(k)$  corresponds to the standard deviation from the distribution of  $P(k)$  measured over all individual skewers and  $N_{ind}(k) = (2\pi)^{-2}(ku_{max})^2$  is the number of independent skewers that can be drawn from the simulation grid for each axis. Applying the Central Limit Theorem,  $\sigma(k)/\sqrt{N_{ind}(k)}$  is analogous to the standard deviation  $\sigma_s(k)$  of the distribution that results from sampling the mean FPS  $\overline{P(k)}$  over all the possible groups of independent skewers, therefore  $\sigma_s(k) \simeq \sigma(k)/\sqrt{N_{ind}(k)}$  provides the uncertainty in the mean FPS measured from the simulation grid.

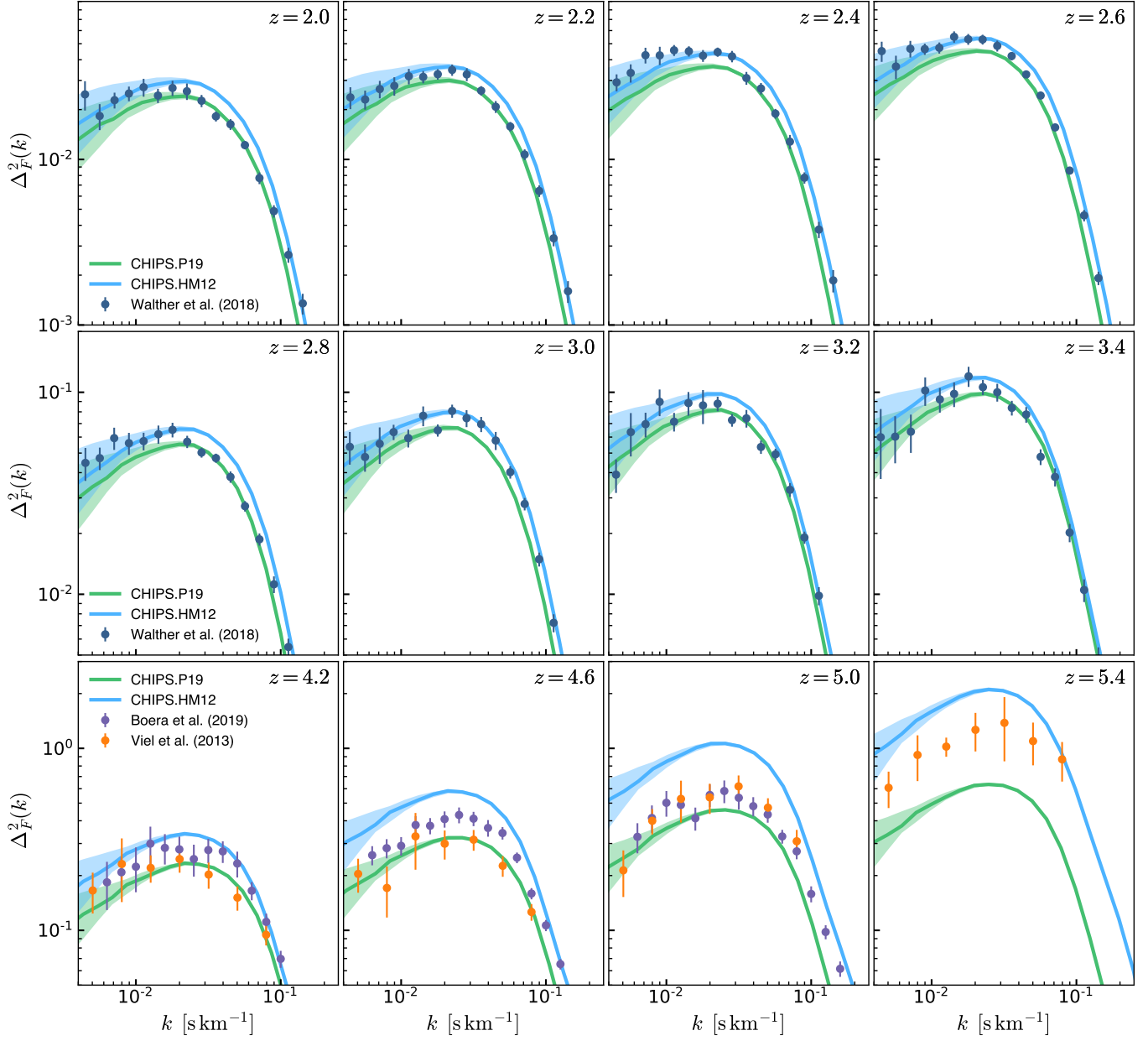


**Figure 15.** One dimensional power spectra of the Lyman- $\alpha$  transmitted flux fluctuations (FPS) from our two simulations CHIPS.HM12 (blue) and CHIPS.P19 (green), compared with the observational measurements from Walther et al. (2018), Boera et al. (2019) and Viel et al. (2013) (data points). The colored lines show the FPS averaged over all the skewers, and the shaded regions show the  $\sigma(k)/\sqrt{N_{\text{ind}}}$  region where  $\sigma(k)$  is the standard deviation of the distribution  $P(\Delta_F^2)$  obtained from the FPS of the all the individual skewers and  $N_{\text{ind}}(k)$  is the number of independent skewers that can be drawn from the simulation grid for each axis. For  $k \gtrsim 0.01 \text{ s km}^{-1}$  the agreement between CHIPS.P19 and the observational measurement of  $P(k)$  for  $2 \lesssim z \lesssim 4.5$  is relatively good (time-averaged  $\langle \chi_\nu^2 \rangle \sim 2$ ), as compared with CHIPS.HM12 ( $\langle \chi_\nu^2 \rangle \sim 8$ ). For  $z \gtrsim 5$  the amplitude of  $P(k)$  for the P19 UVB model is lower than the data, reflecting the lower estimate of  $\tau_{\text{eff}}$  from the P19 model relative to the observations. For  $k \lesssim 0.01 \text{ s km}^{-1}$  the resulting FPS from the HM12 model is in better agreement with the data from Walther et al. (2018) at  $z \lesssim 3$  ( $\langle \chi_\nu^2 \rangle \sim 1$ ) in contrast to the P19 model ( $\langle \chi_\nu^2 \rangle \sim 3$ ).

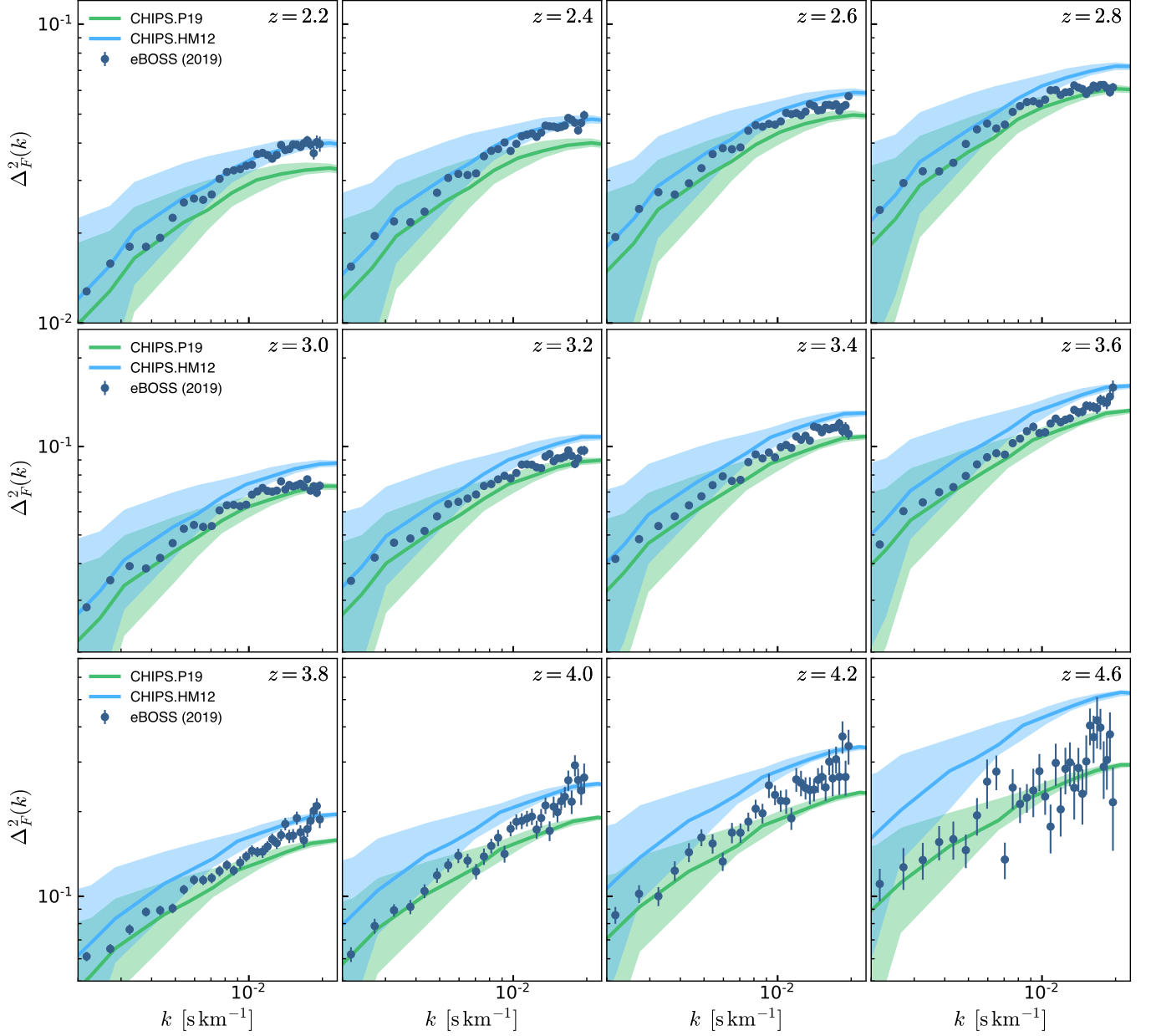


**Figure 16.** One dimensional power spectra of the Lyman- $\alpha$  transmitted flux fluctuations (FPS) from our two simulations CHIPS.HM12 (blue) and CHIPS.P19 (green), compared with the large scale power spectra data from the eBOSS experiment (Chabanier et al. 2019). The colored lines show the FPS averaged over all the skewers, and the shaded regions show the  $\sigma(k)/\sqrt{N_{\text{ind}}}$  region where  $\sigma(k)$  is the standard deviation of the distribution  $P(\Delta_F^2)$  obtained from the FPS of the all the individual skewers and  $N_{\text{ind}}(k)$  is the number of independent skewers that can be drawn from the simulation grid for each axis. From  $z = 2.2$  to  $z = 4.6$  the amplitude of  $P(k)$  for the models increases faster than the data, and for the range  $2.6 \lesssim z \lesssim 4.2$  the data lie in between the models. The P19 and HM12 models result in  $P(k)$  that match the data at  $z = 4.6$  and  $z = 2.2$ , respectively.

The flux power spectrum on scales of  $0.004 < k < 0.2 \text{ s km}^{-1}$  is presented in Figure 15, as shown, the uncertainty bars in the in the power spectrum from the simulations are larger for smaller  $k$  values as the number of independent skewers that can be drawn from the grid decreases as the size of the probed fluctuation increases. We compare the simulation results against observational measurements from Walther et al. (2018) at  $2 < z < 3.4$ , and higher redshift measurements from Boera et al. (2019) and Hiss et al. (2018) for  $4 \lesssim z \leq 5.4$ . To assess the performance of both photoionization and photoheating models to reproduce the observed FPS, we quantify the differences in  $P(k)$  with the statistic  $\chi_\nu^2 = \chi^2/N$ , where

$$\chi^2 = \sum_i^N \left[ \frac{P(k_i)^{\text{obs}} - P(k_i)^{\text{model}}}{\sigma_i^{\text{obs}}} \right]^2, \quad (54)$$

and  $N$  is the number of observed data points measured at the wavenumbers  $k_i$  and having uncertainties  $\sigma_i$ . We will use  $\chi^2$  to denote the statistic computed by Equation 54 for multiple scales at the same redshift, and  $\langle \chi^2 \rangle$  to denote a “time-averaged” statistic when using multiple scales over multiple redshifts.

For  $k \gtrsim 0.01 \text{ s km}^{-1}$ , the agreement between the CHIPS.P19 simulation (green) and the observational measurement of  $P(k)$  for  $2 \lesssim z \lesssim 4.5$  is relatively good as the time-averaged differences are  $\langle \chi_\nu^2 \rangle \sim 2$ , compared to  $\langle \chi_\nu^2 \rangle \sim 8$  for CHIPS.HM12 (blue). At high redshifts ( $z \gtrsim 5$ ), the observational data lie between the predictions from the two models. This result is consistent with the behavior of  $\tau_{\text{eff}}$  in Figure 14, since the normalization of the transmitted flux fluctuations  $\delta F$  is determined by  $\bar{F}$  and an underestimate of  $\tau_{\text{eff}}$  will result in a lower normalization in  $P(k)$ . For  $k \lesssim 0.01 \text{ s km}^{-1}$ , the HM12 UVB model produces FPS that agree better with the data from Walther et al. (2018) at  $z \lesssim 3$  ( $\langle \chi_\nu^2 \rangle \sim 1$ ) than the P19 model ( $\langle \chi_\nu^2 \rangle \sim 3$ ). At high redshift ( $z \gtrsim 4.6$ ), the HM12 model results in a FPS higher than the observations, and this discrepancy is again consistent with the higher values of  $\tau_{\text{eff}}$  produced by the model compared with the observations, as shown in Figure 14.

For larger scales  $0.002 < k < 0.02 \text{ s km}^{-1}$ , the flux power spectrum shown in Figure 16 is compared with the observational measurements from the eBOSS experiment presented in Chabanier et al. (2019). The evolution of  $P(k)$  in CHIPS.HM12 (blue) and CHIPS.P19 (green) differs from the observed data, with the amplitude of  $P(k)$  in the models increasing faster than the data at  $z = 2.2 - 4.6$ . Figure 16 shows that at higher redshift ( $z \sim 4.6$ ) the P19 model  $P(k)$  matches the observations ( $\chi_\nu^2 = 1.4$ ), while for the redshift range  $2.6 \lesssim z \lesssim 4.2$  the data lies in between the models. For

$z \lesssim 2.4$ , the HM12 model agrees better with the data measured by the eBOSS experiment but the small uncertainties in the observational measurements result in large values of  $\chi_\nu^2$  regardless. Since the temperature of the IGM at  $z \lesssim 4$  is primarily set by He II reionization, we argue that the discrepancies between the P19 results and the observed data could be alleviated by changing the He II photoheating rate associated with active galactic nuclei to reduce the IGM temperature at  $z \sim 3$ .

Comparing Lyman- $\alpha$  flux power spectrum between simulations and observation offers a direct way to assess the performance of the chosen photoionization and photoheating rates in reconstructing the thermal history of the IGM. Figures 15 and 16 show that both photoionization and photoheating models used for this work, Haardt & Madau (2012) and Puchwein et al. (2019), fail to recover the observed  $P(k)$  on scales of  $0.002 < k < 0.2 \text{ s km}^{-1}$  over the redshift range  $2 \lesssim z \lesssim 5$ . The observed Lyman- $\alpha$  forest statistics  $\tau_{\text{eff}}$  and  $P(k)$  lie in between the results produced by the two models. This tension motivates further studies using cosmological simulations with modified photoionization and photoheating rates that result in lower IGM temperatures at  $2 < z \lesssim 3$  and increase the amplitude of the FPS on large scales (e.g.,  $0.002 \lesssim k \lesssim 0.02 \text{ s km}^{-1}$ ) to match better the observations.

## 6. DISCUSSION

By comparing the results of our simulations with observations, we have demonstrated the broad properties of the forest are reproduced by models using either the Haardt & Madau (2012) or Puchwein et al. (2019) photoheating and photoionization rates. The Puchwein et al. (2019) rates in particular lead to realistic small-scale structure in the forest over a range in redshift. However, both models fail to recover the detailed shape of the transmitted flux  $P(k)$  or the magnitude of the optical depth at all redshifts or spatial scales. The physical reasons for these inadequacies likely also depend on redshift and spatial scale, and are discussed below.

### 6.1. What is the IGM Photoheating History?

As Figures 11 and 12 illustrate, the observational inferences on the evolution of the IGM mean temperature and density-temperature relation are currently widely-varying (Hiss et al. 2018; Bolton et al. 2014; Walther et al. 2018; Boera et al. 2019; Gaikwad et al. 2020b,a). Deriving these observed properties requires assistance from simulations, for instance by generating model spectra or aiding the interpretation of transmission spikes. As a result, discriminating between early-reionization (Haardt & Madau 2012) and late-reionization (Puch-

wein et al. 2019) based on  $T_0(z)$  and  $\gamma(z)$  remains hazardous. The Lyman- $\alpha$  optical depth and  $P(k)$  evolution show that the observations mostly reside in between the model predictions. At redshifts  $z \sim 2 - 3$  the Puchwein et al. (2019) rates produce structure in the forest that agrees better with the data on small scales, but on larger scales Haardt & Madau (2012) performs better. The IGM structure at these redshifts is heavily influenced by He II photoheating powered by active galactic nuclei, and both the relative spectral slopes of the AGN spectral energy distribution and the difference in emissivity with redshift in these models could affect their scale-dependent relative agreement. Finding the He II photoheating and photoionization rates that result in agreement across all scales at these redshifts will require future work and more simulations.

Close to the hydrogen reionization era, in simulations using the Haardt & Madau (2012) rates the Lyman- $\alpha$   $P(k)$  amplitude increases more rapidly with redshift than in the Puchwein et al. (2019) model. Reionization occurs very early in the Haardt & Madau (2012) UVB, and the  $P(k)$  amplitude evolution reflects the progressively colder IGM in this scenario. The hydrogen ionization and temperature states of the IGM in the Puchwein et al. (2019) model are apparently too high, and produce a lower  $P(k)$  than seen in the observation. Balancing the high temperature resulting from the late reionization in this model and the larger  $P(k)$  may require a patchy reionization process, as noted previously (Keating et al. 2020).

## 6.2. IGM Thermal History vs. Instantaneous Properties

The importance of developing self-consistent histories for IGM properties, including the phase structure, flux power spectra, and Lyman- $\alpha$  optical depth, cannot be overstated for interpreting observations. The power of the Lyman- $\alpha$  forest for constraining the small-scale physics of structure formation, including the possible presence of warm dark matter (e.g., Viel et al. 2013; Iršič et al. 2017) and the importance of neutrinos (e.g., Chabanier et al. 2019), is limited by the imprecisely known thermal properties that can impact such scales. These uncertainties on the thermal properties, often characterized by the temperature  $T_0$  at the mean density and the slope  $\gamma$  of the IGM temperature-density relation, have frequently been treated as nuisance parameters when developing cosmological parameter constraints from the Lyman- $\alpha$  forest. Analyses typically marginalize over the uncertainties in the thermal structure of the forest to arrive at, e.g., the possible contribution of warm dark matter to the suppression of small-scale power.

One complication with these analyses that our simulations highlight is how the history and evolution of the thermal properties influence the structure of the forest. The characteristics of the forest at one redshift cannot be disentangled entirely from its properties at similar redshifts. The response of the forest, in terms of both its thermal and ionization structure, depends on the evolving photoheating and photoionization rates, and the values of both  $T_0$  and  $\gamma$  change along tracks with redshift. These properties are not independent, and have redshift correlations that cannot be ignored by separately marginalizing over their properties independently at an array of redshifts. Instead, when marginalizing over the thermal structure of the forest to infer constraints from  $P(k)$ , full simulated histories of the forest properties are required with marginalization occurring simultaneously over the forest structure at all redshifts where observations are available. For instance, synthesizing the results shown in Figures 11, 12, 15, we find that the consistently lower  $P(k)$  amplitude of the forest at  $z = [4.2, 4.6, 5.0, 5.4]$  when using the Puchwein et al. (2019) rates results from the hotter IGM induced by the late global reionization in this model. The temperature at these times is not independent across redshift, and varying models over a range of IGM temperature and Lyman- $\alpha$   $P(k)$  at a given redshift amounts to direct assumptions on those properties at adjacent redshifts where the dominant photoheating mechanisms are the same.

Addressing this issue requires a potentially large number of hydrodynamical simulations of cosmological structure formation that capture various photoheating histories and manage to resolve the Lyman- $\alpha$  forest structure robustly on small scales. Our CHIPS simulations represent a first step in this direction, and the computational efficiency of the *Cholla* code will enable us to realize the required number of simulations with moderate additional effort.

## 7. SUMMARY

Motivated by new observational efforts that will provide unprecedented detail on the properties of the Lyman- $\alpha$  forest (e.g., DESI Collaboration et al. 2016a), we have initiated the CHIPS series of hydrodynamical simulations of cosmological structure formation. Our simulations use the GPU-native *Cholla* code to maintain exquisite spatial resolution in the low-density intergalactic medium throughout cosmological volumes. In this first paper, we conduct  $N = 2048^3$  resolution simulations to compare the thermal history and physical properties of the Lyman- $\alpha$  forest using two models for the photoheating and photoionization rates induced by



an evolving ultraviolet background (Haardt & Madau 2012; Puchwein et al. 2019). A summary of our efforts and conclusions follows.

- We extended the *Cholla* code to perform cosmological simulations by engineering gas self-gravity, a Fourier-space Poisson solver, a particle integrator, a comoving coordinate scheme, and a coupling to the GRACKLE heating and cooling library (Smith et al. 2017).
- We provided extensive tests of our cosmological simulations, including the Zel'Dovich (1970) pancake test and comparisons with the results of other cosmological simulation codes. *Cholla* agrees with *Nyx* (Almgren et al. 2013), *Ramses* (Teyssier 2002), and *Enzo* (Bryan et al. 2014) to sub-percent accuracy on all spatial scales for N-body cosmological simulations, and matches *Ramses* and *Enzo* results to within a few percent for adiabatic hydrodynamical simulations.
- We provide a new method for testing the dual energy formalism (Bryan et al. 1995) of Eulerian hydrodynamical codes for cosmological simulations by matching the mean cosmic gas temperature in adiabatic simulations, and show that *Cholla* recovers the expected results.
- In accordance with prior results (e.g., Puchwein et al. 2019), we find that after hydrogen reionization, simulations using the Haardt & Madau (2012) photoheating rates predict a cooler IGM temperature than the Puchwein et al. (2019) UVB model. At redshifts  $z \sim 4 - 6$ , the Puchwein et al. (2019) model is hotter owing to hydrogen reionization completing later than in the Haardt & Madau (2012) scenario. At redshifts  $z \lesssim 4$ , the IGM is hotter in the Puchwein et al. (2019) model owing to the He II photoheating rates powered by active galactic nuclei.
- We compare the Lyman- $\alpha$  transmitted flux power spectra  $P(k)$  computed for these simulations with observations. We find that at redshifts  $2 \lesssim z \lesssim 5.5$  the performance of the models varies with scale. Using the Puchwein et al. (2019) photoheating rates results in good agreement with the observed  $P(k)$  on  $k \gtrsim 0.01 \text{ s km}^{-1}$  at  $2 \lesssim z \lesssim 4.5$ .
- On larger scales, the amplitude of the observed  $P(k)$  increases faster from  $z \sim 2.2$  to  $z \sim 4.6$  than the structure in the simulated forest. The observations appear intermediate between the simulation results using the Haardt & Madau (2012)

and Puchwein et al. (2019) photoheating rates at  $2.2 \lesssim z \lesssim 4.6$  for  $k \approx 0.002 - 0.01 \text{ s km}^{-1}$ .

- At higher redshifts  $z \gtrsim 4.5$ , as the epoch of hydrogen reionization is approached, the  $P(k)$  amplitude in the simulations increase at rates that bracket the observed flux  $P(k)$ . The observed Lyman- $\alpha$  optical depth also lies in between the model predictions at these redshifts.
- We show that our results are insensitive to small changes in the cosmological parameters comparable to the Planck Collaboration et al. (2018) uncertainties, and demonstrate our results for the flux power spectra have converged with resolution studies.

These initial CHIPS simulations demonstrate that commonly used models for the photoheating and photoionization rates (Haardt & Madau 2012; Puchwein et al. 2019) broadly reproduce the observed thermal history and transmitted flux power spectra of the Lyman- $\alpha$  forest. However, in detail the agreement with the observations can be improved, including better recovering the redshift- and scale-dependence of the the flux  $P(k)$  and the evolution in the Lyman- $\alpha$  optical depth. Matching these observations more completely will require changing the photoionization and photoheating rates for both hydrogen and helium. We will explore these improvements using additional large-scale cosmological simulations in future work.

We wish to thank Francesco Haardt and Ewald Puchwein for their discussions and guidance. The simulations used for this paper were produced in the Summit system (ORNL) project AST149. This research used resources of the Oak Ridge Leadership Computing Facility at the Oak Ridge National Laboratory, which is supported by the Office of Science of the U.S. Department of Energy under Contract No. DE-AC05-00OR22725. We acknowledge use of the *lux* supercomputer at UC Santa Cruz, funded by NSF MRI grant AST 1828315. Bruno Villaseñor is supported in part by the UC MEXUS-CONACyT doctoral fellowship. BER acknowledges support from NASA contract NNG16PJ25C and grant 80NSSC18K0563. We acknowledge the comments and suggestions received from the paper referee which helped improve the content and clarity of this work.

*Software:* *Cholla* (Schneider & Robertson 2015, <https://github.com/cholla-hydro/cholla>), Python (van Rossum 1995), Numpy (Van Der Walt et al. 2011), Matplotlib (Hunter 2007), MUSIC (Hahn & Abel 2011),

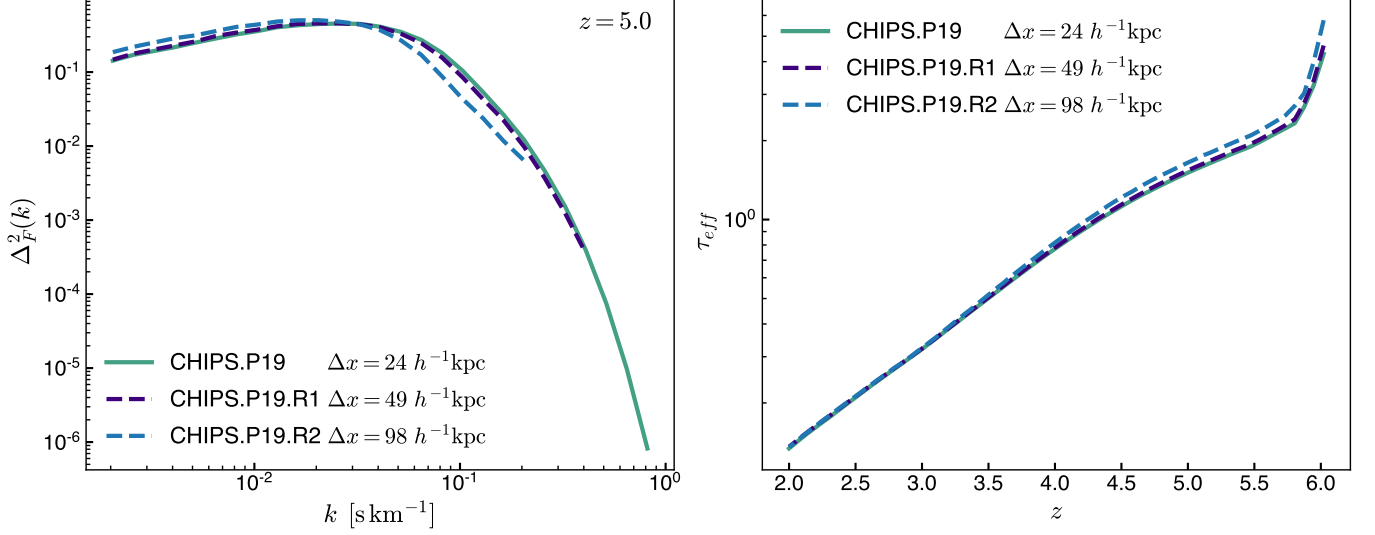


**Figure 17.** Lyman- $\alpha$  forest statistics measured for similar simulations with different spatial resolutions  $\Delta x = 98, 49$  and  $24 h^{-1} \text{kpc}$  (comoving). All simulations have  $L = 50 h^{-1} \text{Mpc}$  and use the Puchwein et al. (2019) UVB model and Planck Collaboration et al. (2018) cosmological parameters. The transmitted flux power spectrum  $\Delta_F^2$  at  $z = 5$  is shown in the left panel and the redshift evolution of the effective optical depth  $\tau_{eff}$  is shown on the right. Both measurements demonstrate that the relevant statistics of the Lyman- $\alpha$  forest have converged for the high resolution simulations used in this work.

PFFT (Pippig 2013), GRACKLE (Smith et al. 2017),

CLOUDY (Ferland et al. 2017), ROCKSTAR (Behroozi et al. 2013).

## APPENDIX

### A. RESOLUTION CONVERGENCE ANALYSIS

To assess the numerical convergence of our results, we performed runs with different resolutions. Each simulation was run with the same box size ( $L = 50 h^{-1} \text{Mpc}$ ) and identical cosmological parameters (Planck Collaboration et al. 2018), but with differing resolutions of  $N = 512^3$ ,  $N = 1024^3$ , and  $N = 2048^3$  cells and dark matter particles. These simulations have comoving spatial resolutions of  $\Delta x = 98, 49$ , and  $24 h^{-1} \text{kpc}$ , respectively. The initial conditions were generated to preserve the large-scale modes in common to each simulation, such that the properties of the simulations could be compared directly on shared spatial scales. We measured the Lyman- $\alpha$  effective optical depth and transmitted flux power spectrum at each resolution.

The left panel of Figure 17 shows the convergence of the Lyman- $\alpha$  transmitted flux power spectra with resolution. As the resolution increases, the large-scale  $P(k)$  decreases while the small-scale power increases. This progression reflects the structure of the forest becoming better resolved as the number of cells increases. The  $N = 1024^3$  and  $N = 2048^3$  simulations agree well over most spatial scales, with little evidence that the  $N = 2048^3$  simulation requires further refinement on scales  $k \gtrsim 0.007 \text{ s km}^{-1}$ .

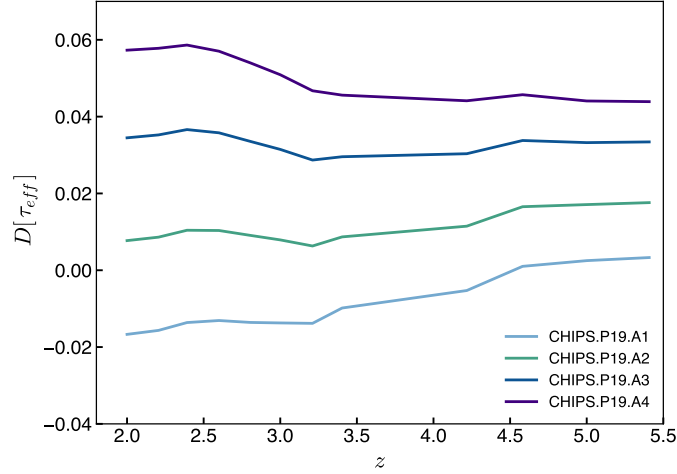
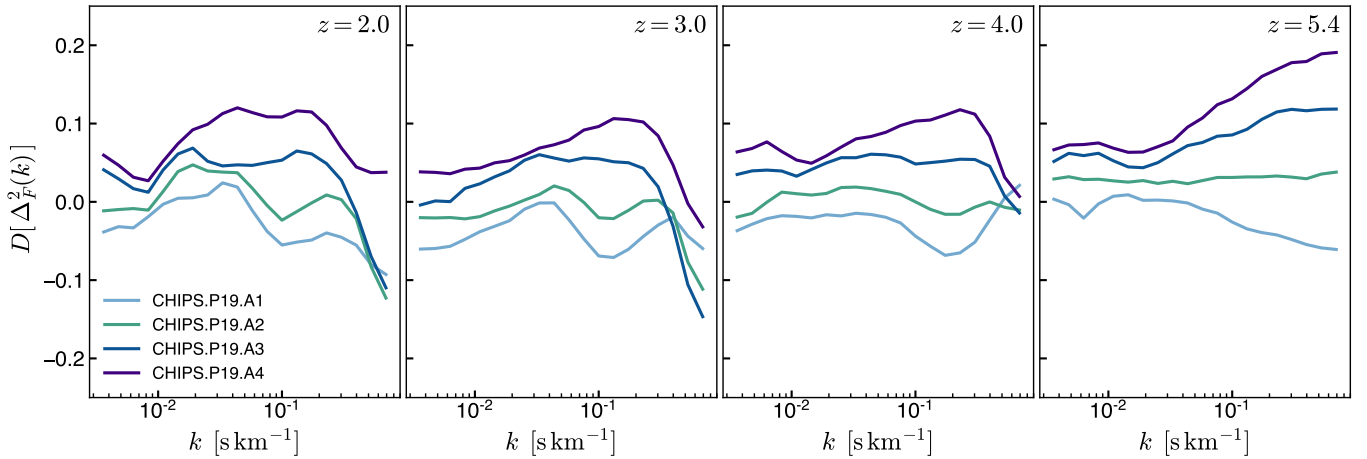
The right panel of Figure 17 details the redshift evolution of the Lyman- $\alpha$  optical depth measured in the convergence study. As the structure of the forest becomes better resolved, the optical depth lowers. This decline reflects the decrease in large-scale power as the resolution improves, as illustrated in the left panel of Figure 19. As with the  $P(k)$  analysis, the  $N = 1024^3$  and  $N = 2048^3$  simulations agree well in their Lyman- $\alpha$  optical depth evolution. The large-scale structure of the forest also agrees well between these simulations, demonstrating that the  $N = 2048^3$  simulations have converged on scales that most contribute to the optical depth.

### B. COSMOLOGICAL PARAMETER STUDY

The relative difference in the Lyman- $\alpha$  forest properties between simulations using the Haardt & Madau (2012) or Puchwein et al. (2019) rates is substantial, but understanding whether these differences are large compared differences in the forest resulting from cosmological parameter variations requires further simulation. To answer this question we repeated our highest resolution simulation using the Puchwein et al. (2019) rates with a range of cosmological

**Table 2.** Mean Gas Density Comparison for Alternative Cosmologies

Simulation	Mean baryon density $\bar{\rho}_b$ [ $M_\odot \text{kpc}^{-3}$ ]	$\Delta \bar{\rho}_b / \bar{\rho}_b$ [ $\times 10^{-2}$ ]
CHIPS.P19	6.315	
CHIPS.P19.A1	6.275	-0.62
CHIPS.P19.A2	6.334	0.31
CHIPS.P19.A3	6.394	1.25
CHIPS.P19.A4	6.449	2.12

**Figure 18.** Redshift-dependent fractional difference of the effective optical depth  $\tau_{eff}$  in the alternative cosmology simulations, measured with respect to the fiducial CHIPS.P19 simulation that evolves a [Planck Collaboration et al. \(2018\)](#) cosmology. The variations in  $\tau_{eff}$  reflect differences in the mean baryonic density  $\bar{\rho}_b$  for the alternative cosmologies shown in Table 2.**Figure 19.** Fractional differences in the flux power spectra  $\Delta_F^2$  of the alternative cosmology simulations. The differences are measured with respect to the fiducial CHIPS.P19 simulation that evolves a [Planck Collaboration et al. \(2018\)](#) cosmology (shown for redshifts  $z = [2, 3, 4, 5.4]$ ). The differences are scale dependent, and the overall variations in normalization reflect the differences in  $\tau_{eff}$  shown in Figure 18.

parameters, varying over the reported uncertainty in the [Planck Collaboration et al. \(2018\)](#) analysis. We ran four simulations where we varied the Hubble parameter  $H_0$ , matter density  $\Omega_m$ , baryon density  $\Omega_b$ , RMS fluctuations on  $8 h^{-1}\text{Mpc}$  scales  $\sigma_8$ , and the spectral slope of initial perturbations  $n_s$ . The chosen numerical values of the cosmological parameters are reported in Table 1.

Table 2 shows the mean comoving baryonic density  $\bar{\rho}_b$  for the reference simulation CHIPS.P19 and the simulations with alternative cosmologies. Additionally, for the alternative cosmologies the fractional difference of the average density  $\Delta\bar{\rho}_b/\bar{\rho}_b$  relative to the reference CHIPS.P19 is shown in the second column. The differences in the mean gas density are approximately a few percent and reflect differences in the mean optical depth measured in the alternative cosmology simulations with respect to the CHIPS.P19 simulation. The differences in the effective optical depth  $D[\tau_{eff}]$  relative to CHIPS.P19 as a function of redshift are shown in Figure 18. The differences in  $\tau_{eff}$  range from -2% to 6%, exhibit little evolution with redshift, and cannot, e.g., account for the deviations of  $\tau_{eff}$  resulting from the [Puchwein et al. \(2019\)](#) model and the observational measurements shown in Figure 14.

Figure 19 shows the resulting variation in the transmitted flux  $P(k)$  induced by the small variations introduced in the cosmological parameters. The differences in the power spectrum  $D[\Delta_F^2]$  relative to the reference CHIPS.P19 are shown for four snapshots at redshifts between  $z = 2.0$  and  $z = 5.4$ . The differences in  $P(k)$  are scale dependent, but are consistent with the differences shown in Figure 18 for  $\tau_{eff}$  as the mean transmitted flux  $\bar{F}$  sets the normalization of  $P(k)$ . To disentangle the effect that varying each cosmological parameter has on the Lyman- $\alpha$  statistics a more extensive study would have to be performed, but we conclude the overall effect of the cosmological variations is small and as Figure 19 demonstrates, the difference in physical structure between simulations conducted with the [Haardt & Madau \(2012\)](#) or [Puchwein et al. \(2019\)](#) rates cannot be easily mimicked with cosmological parameter variations allowed by experimental constraints. This result also emphasizes the need to account for the IGM thermal history when inferring cosmological properties from the forest.

We also compared the evolution of the thermal parameters  $T_0$  and  $\gamma$  from the alternative cosmology simulations to the reference CHIPS.P19 simulation, and found that the differences in  $T_0$  and  $\gamma$  relative to the [Planck Collaboration et al. \(2018\)](#) cosmology were  $\lesssim 3\%$ . Since these differences are of the order of the uncertainties resulting from modeling the density-temperature distribution as a power-law relation (Equation 43), we do not report any significant variation in the thermal history of the IGM owing to small variations of the cosmological parameters.

## REFERENCES

- Almgren, A. S., Bell, J. B., Lijewski, M. J., Lukić, Z., & Van Andel, E. 2013, *ApJ*, 765, 39
- Arinyo-i-Prats, A., Miralda-Escudé, J., Viel, M., & Cen, R. 2015, *Journal of Cosmology and Astro-Particle Physics*, 2015, 017
- Becker, G. D., Hewett, P. C., Worseck, G., & Prochaska, J. X. 2013, *MNRAS*, 430, 2067
- Behroozi, P. S., Wechsler, R. H., & Wu, H.-Y. 2013, *ApJ*, 762, 109
- Boera, E., Becker, G. D., Bolton, J. S., & Nasir, F. 2019, *ApJ*, 872, 101
- Bolton, J. S., Becker, G. D., Haehnelt, M. G., & Viel, M. 2014, *MNRAS*, 438, 2499
- Bosman, S. E. I., Fan, X., Jiang, L., et al. 2018, *MNRAS*, 479, 1055
- Bryan, G. L., Norman, M. L., Stone, J. M., Cen, R., & Ostriker, J. P. 1995, *Computer Physics Communications*, 89, 149
- Bryan, G. L., Norman, M. L., O’Shea, B. W., et al. 2014, *The Astrophysical Journal Supplement Series*, 211, 19
- Cen, R., Miralda-Escudé, J., Ostriker, J. P., & Rauch, M. 1994, *ApJL*, 437, L9
- Chabanier, S., Palanque-Delabrouille, N., Yèche, C., et al. 2019, *JCAP*, 2019, 017
- Colella, P., & Woodward, P. R. 1984, *Journal of Computational Physics*, 54, 174
- D’Aloisio, A., McQuinn, M., Davies, F. B., & Furlanetto, S. R. 2018, *Monthly Notices of the Royal Astronomical Society*, 473, 560
- D’Aloisio, A., McQuinn, M., Maupin, O., et al. 2019, *Astrophysical Journal*, 874, 154
- D’Aloisio, A., Upton Sanderbeck, P. R., McQuinn, M., Trac, H., & Shapiro, P. R. 2017, *Monthly Notices of the Royal Astronomical Society*, 468, 4691
- Davies, F. B., Hennawi, J. F., Eilers, A.-C., & Lukić, Z. 2018a, *Astrophysical Journal*, 855, 106
- Davies, F. B., Hennawi, J. F., Bañados, E., et al. 2018b, *Astrophysical Journal*, 864, 142
- DESI Collaboration, Aghamousa, A., Aguilar, J., et al. 2016a, *arXiv e-prints*, arXiv:1611.00036
- . 2016b, *arXiv e-prints*, arXiv:1611.00037



- Doussot, A., Trac, H., & Cen, R. 2019, *Astrophysical Journal*, 870, 18
- Eilers, A.-C., Davies, F. B., Hennawi, J. F., et al. 2017, *ApJ*, 840, 24
- Faucher-Giguère, C.-A. 2020, *MNRAS*, 493, 1614
- Ferland, G. J., Chatzikos, M., Guzmán, F., et al. 2017, *RMxAA*, 53, 385
- Gaikwad, P., Srianand, R., Haehnelt, M. G., & Choudhury, T. R. 2020a, arXiv e-prints, arXiv:2009.00016
- Gaikwad, P., Rauch, M., Haehnelt, M. G., et al. 2020b, *MNRAS*, 494, 5091
- Garaldi, E., Gnedin, N. Y., & Madau, P. 2019, *Astrophysical Journal*, 876, 31
- Gnedin, N. Y. 2016, *Astrophysical Journal*, 821, 50
- Gnedin, N. Y., Becker, G. D., & Fan, X. 2017, *ApJ*, 841, 26
- Gnedin, N. Y., & Kaurov, A. A. 2014, *Astrophysical Journal*, 793, 30
- Gunn, J. E., & Peterson, B. A. 1965, *ApJ*, 142, 1633
- Haardt, F., & Madau, P. 2012, *ApJ*, 746, 125
- Hahn, O., & Abel, T. 2011, *MNRAS*, 415, 2101
- Hernquist, L., Katz, N., Weinberg, D. H., & Miralda-Escudé, J. 1996, *ApJL*, 457, L51
- Hiss, H., Walther, M., Hennawi, J. F., et al. 2018, *The Astrophysical Journal*, 865, 42
- Hockney, R. W., & Eastwood, J. W. 1988, *Computer simulation using particles* (CRC Press)
- Hui, L., & Gnedin, N. Y. 1997, *MNRAS*, 292, 27
- Hunter, J. D. 2007, *Computing in Science & Engineering*, 9, 90
- Iršič, V., Viel, M., Haehnelt, M. G., et al. 2017, *PhRvD*, 96, 023522
- Kaurov, A. A., & Gnedin, N. Y. 2014, *Astrophysical Journal*, 787, 146
- . 2015, *Astrophysical Journal*, 810, 154
- Keating, L. C., Weinberger, L. H., Kulkarni, G., et al. 2020, *MNRAS*, 491, 1736
- Khaire, V., Walther, M., Hennawi, J. F., et al. 2019, *Monthly Notices of the Royal Astronomical Society*, 486, 769
- Krolewski, A., Lee, K.-G., White, M., et al. 2018, *Astrophysical Journal*, 861, 60
- Kulkarni, G., Hennawi, J. F., Oñorbe, J., Rorai, A., & Springel, V. 2015, *Astrophysical Journal*, 812, 30
- La Plante, P., Trac, H., Croft, R., & Cen, R. 2017, *ApJ*, 841, 87
- . 2018, *ApJ*, 868, 106
- Lukić, Z., Stark, C. W., Nugent, P., et al. 2015, *MNRAS*, 446, 3697
- Madau, P., Haardt, F., & Rees, M. J. 1999, *ApJ*, 514, 648
- Martel, H., & Shapiro, P. R. 1998, *MNRAS*, 297, 467
- McQuinn, M. 2016, *ARA&A*, 54, 313
- Miniati, F., & Colella, P. 2007, *Journal of Computational Physics*, 227, 400
- Oñorbe, J., Hennawi, J. F., & Lukić, Z. 2017a, *ApJ*, 837, 106
- Oñorbe, J., Hennawi, J. F., Lukić, Z., & Walther, M. 2017b, *ApJ*, 847, 63
- Osterbrock, D. E. 1989, *Astrophysics of gaseous nebulae and active galactic nuclei* (University Science Books)
- Pippig, M. 2013, *SIAM Journal on Scientific Computing*, 35, C213
- Planck Collaboration, Aghanim, N., Akrami, Y., et al. 2018, arXiv e-prints, arXiv:1807.06209
- Puchwein, E., Bolton, J. S., Haehnelt, M. G., et al. 2015, *MNRAS*, 450, 4081
- Puchwein, E., Haardt, F., Haehnelt, M. G., & Madau, P. 2019, *MNRAS*, 485, 47
- Rorai, A., Hennawi, J. F., Oñorbe, J., et al. 2017, *Science*, 356, 418
- Schmidt, T. M., Hennawi, J. F., Worsack, G., et al. 2018, *ApJ*, 861, 122
- Schneider, E. E., & Robertson, B. E. 2015, *ApJS*, 217, 24
- . 2017, *ApJ*, 834, 144
- Sheth, R. K., & Tormen, G. 1999, *MNRAS*, 308, 119
- Smith, B. D., Bryan, G. L., Glover, S. C. O., et al. 2017, *MNRAS*, 466, 2217
- Sorini, D., Oñorbe, J., Hennawi, J. F., & Lukić, Z. 2018, *ApJ*, 859, 125
- Teyssier, R. 2002, *A&A*, 385, 337
- Teyssier, R. 2015, *Annual Review of Astronomy and Astrophysics*, 53, 325
- Tonnesen, S., Smith, B. D., Kollmeier, J. A., & Cen, R. 2017, *ApJ*, 845, 47
- Trac, H., Cen, R., & Mansfield, P. 2015, *ApJ*, 813, 54
- Van Der Walt, S., Colbert, S. C., & Varoquaux, G. 2011, *Computing in Science & Engineering*, 13, 22
- van Rossum, G. 1995, *Python tutorial*, Tech. Rep. CS-R9526, Centrum voor Wiskunde en Informatica (CWI), Amsterdam
- Viel, M., Becker, G. D., Bolton, J. S., & Haehnelt, M. G. 2013, *PhRvD*, 88, 043502
- Walther, M., Hennawi, J. F., Hiss, H., et al. 2018, *ApJ*, 852, 22
- Walther, M., Oñorbe, J., Hennawi, J. F., & Lukić, Z. 2019, *ApJ*, 872, 13
- Worsack, G., Prochaska, J. X., Hennawi, J. F., & McQuinn, M. 2016, *ApJ*, 825, 144
- Zel'Dovich, Y. B. 1970, *A&A*, 500, 13